frontiers | Frontiers in Marine Science

TYPE Original Research
PUBLISHED 14 September 2022
DOI 10.3389/fmars.2022.967627

OPEN ACCESS

EDITED BY
Ibon Galparsoro,
Technological Center Expert in Marine and Food Innovation (AZTI), Spain

REVIEWED BY
Pradipta Ranjan Muduli,
Chilika Development Authority, India
Adriana Gonzalez Silvera,
Universidad Autónoma de Baja California, Ensenada, Mexico

*CORRESPONDENCE
Nivedita Sanwlani
nsanwlani@ntu.edu.sg

†PRESENT ADDRESS
Elizabeth Wing-See Wong,
Synspective SG Pte. Ltd., Singapore

SPECIALTY SECTION
This article was submitted to Marine Ecosystem Ecology, a section of the journal Frontiers in Marine Science

RECEIVED 13 June 2022
ACCEPTED 22 August 2022
PUBLISHED 14 September 2022

CITATION
Sanwlani N, Wong EW-S, Morgan K, Liew SC and Martin P (2022) Inherent Optical Properties based Vulnerability Assessment of Euphotic Zone Compression in peatland influenced Southeast Asian coastal waters. *Front. Mar. Sci.* 9:967627. doi: 10.3389/fmars.2022.967627

Inherent Optical Properties based Vulnerability Assessment of Euphotic Zone Compression in peatland influenced Southeast Asian coastal waters

Nivedita Sanwlani[1,2]*, Elizabeth Wing-See Wong[3]†, Kyle Morgan[2,4], Soo Chin Liew[3] and Patrick Martin[2]

[1]Nanyang Environment & Water Research Institute, Nanyang Technological University, Singapore, Singapore, [2]Asian School of the Environment, Nanyang Technological University, Singapore, Singapore, [3]Centre for Remote Imaging, Sensing, and Processing, National University of Singapore, Singapore, Singapore, [4]Earth Observatory of Singapore, Nanyang Technological University, Singapore, Singapore

Underwater light availability is a crucial aspect for the ecological functioning of shallow water bodies. Light extinction from terrestrial inputs is a growing threat to these coastal habitats. The blended quasi-analytical algorithm (QAA) was extended for the derivation of colored dissolved organic matter (CDOM) absorption coefficient along with other inherent optical properties (IOPs) from satellite observations for Southeast Asian waters. The contribution of these IOPs to diffuse attenuation of light (K_d) and penetration depth (Z_d) was investigated. A vulnerability assessment was performed to identify locations potentially threatened by poor light quality in Southeast Asian waters. Advection of peatland-influenced Sumatran coastal waters rich in organic matter (a_g(400nm): 1.0-2.0m^{-1}) and sediments (b_{bp}(400nm): 0.5-1m^{-1}) drive the spatial heterogeneity of Sunda shelf seawater. Photic zone depth, Z_d (490nm), is year-round restricted to ≤5m for critically vulnerable Sumatran coastal waters (vulnerability index, VI>0.8). This critically vulnerable state is further extended towards the southern Malacca Strait, influencing the eastern Singapore Strait from June to September. The areas harbouring marine ecosystems in the shelf waters attain a higher threshold (VI=0.6-0.8), constraining the photosynthesis to depths ≤10m. A transformation of central Malacca Strait from not vulnerable (VI<0.2) to highly vulnerable (VI=0.6-0.8) state from June to September indicates poor light conditions. Further increases in CDOM and sediment inputs into these water columns, therefore, constitute a clear risk of reducing light availability, which may have damaging effects on the functioning of coastal habitats. This study underscores the need for a complete ecological risk assessment for Southeast Asia to aid in the effective management of marine ecosystems.

KEYWORDS

diffuse attenuation coefficient, photic zone depth, vulnerability assessment, Southeast Asia, peatland run-off, CDOM

Introduction

Southeast Asia's (SEA's) carbon-rich peatlands are recognized as a major source of fluvial dissolved organic carbon (DOC) fluxes to coastal waters (Moore et al., 2011). Sumatran and Bornean coastal peatlands together store around 69 Pg C of terrestrial organic carbon (Page et al., 2011; Dommain et al., 2014) and contribute ~10% of the annual global land-ocean terrestrial DOC (tDOC) flux (Baum et al., 2007; Moore et al., 2011). Although the release of carbon from peatlands is a natural process, the rising demand for lucrative agricultural practices has accelerated deforestation, intensive burning, and hydrological disturbances in Southeast Asia (Miettinen et al., 2016; Vadrevu et al., 2019). More than 90% of Southeast Asian peatlands have been drained, deforested, and primarily converted to agricultural use in the past two to three decades (Miettinen et al., 2016). This ongoing anthropogenic disturbance on peatlands is potentially extended into the marine environment by increasing the fluvial tDOC export by possibly ~50% (Moore et al., 2013; Yupi et al., 2016; Sanwlani et al., 2022). The majority of the exported tDOC from the peatlands on Sumatra and Borneo appears to be remineralized within the shelf sea (Wit et al., 2018; Zhou et al., 2021), although the processes driving this remineralization and the rates at which it occurs remain unclear. However, a significant proportion (around 20–30%) appears to be relatively refractory and likely survives its passage through the shelf sea (Zhou et al., 2021).

The DOC that originates from terrestrial environments is particularly enriched in colored dissolved organic matter (CDOM), and field surveys have revealed conservative mixing and transport of organic matter across the salinity gradients (Fichot and Benner, 2012; Martin et al., 2018; Zhou et al., 2019). CDOM, also known as gelbstoff, is tannin-rich material, often generated by the partial degradation of terrestrial or marine organic matter that influences the biogeochemistry of the marine ecosystem (Coble, 2007). Optical remote sensing has played an indispensable role in measuring the large-scale optically active fraction of DOC (CDOM) and suspended sediments in a range of coastal environments (Fichot and Benner, 2014; Mannino et al., 2014; Joshi et al., 2017). Algorithms to retrieve CDOM and DOC from the remotely sensed surface water spectrum are now readily available at global-scale for open-ocean waters (Nelson and Siegel, 2013; Aurin et al., 2018), while regionally parameterized and adequately validated algorithms are available for coastal waters (Fichot et al., 2013; Joshi et al., 2017; Cao et al., 2018; Liu et al., 2019; Signorini et al., 2019). However, there is a lack of tools to infer and monitor CDOM and, by inference DOC, in Southeast Asian waters that receive some of the highest global rates of terrestrial organic carbon inputs.

CDOM is a major component responsible for the attenuation of light that plays a crucial role in influencing the aquatic light regime (Vantrepotte et al., 2015; Oestreich et al., 2016). It absorbs a substantial fraction of ultraviolet (UV) and photosynthetically available radiation (PAR) that aids in controlling the penetration of sunlight in the water column, thereby reducing UV exposure of marine biota and organisms and protecting them from direct DNA damage (Pienitz and Vincent, 2000). However, the attenuation of PAR in the water column can also negatively affect the primary productivity of plankton and benthic ecosystems, especially coral reefs, that require high amounts of light for their growth and physiological functioning (Gattuso et al., 2006). The reduction in underwater light contributes significantly to changes in coral and phytoplankton species composition, abundance, and morphology, leading to vertical reef compression (Kramer et al., 2020; Morgan et al., 2020). The availability of light is vital for the ecological functioning of shallow water bodies such as the Sunda Shelf Sea. The Sunda Shelf Sea has been the focus of considerable attention for receiving elevated terrestrial fluxes due to the large-scale anthropogenic changes (Moore et al., 2011; Miettinen et al., 2016; Yupi et al., 2016; Zhou et al., 2021) (Moore et al., 2013; Wit et al., 2018; Sanwlani et al., 2022). Terrestrial run-off from modified catchments can additionally enhance the transport of sediments, minerals, and CDOM that could potentially reduce the amount and compress the depth of penetration of solar radiation to the seabed for seagrass and corals. The high attenuation and poor water quality due to the enhanced terrestrial run-off are considered a threat to coastal ecosystems (Fredston-Hermann et al., 2016; Jones et al., 2021). The effects of photic compression will exacerbate the vulnerability of coastal and marine species, habitats, and ecosystems (Gattuso et al., 2006; Brandao et al., 2017; Jones et al., 2021). Vertically compressed coral depth distributions have been reported in Singapore's turbid reef systems located in the central Sunda Shelf Sea (Morgan et al., 2020). Despite its significance, no risk assessment of reduction in underwater light has been performed so far. And the threats to the aquatic light regime have not been critically examined to the same extent as for other environmental factors such as temperature and salinity. Consequently, the knowledge of light attenuation and its contributing factors influencing tropical shelf seas marine habitats is still limited.

Inherent optical properties (IOPs, absorption and scattering properties of seawater and its constituents) based vulnerability assessment of photic zone compression is performed in this study for SEA coastal turbid waters. Here, we first develop a new algorithm by extending the blended Quasi analytical algorithm (QAA) by (Shi and Wang, 2019) to derive the CDOM absorption coefficient using *in situ* bio-optical datasets acquired in the Singapore Strait and the synthesized IOCCG dataset. The proposed algorithm is then implemented on Sentinel-3a satellite ocean color observations to determine the spatial-seasonal dynamics of IOPs– CDOM absorption coefficient at 400 nm (a measure of CDOM concentration), particulate backscattering coefficient at 400 nm (a measure of

suspended sediment concentration), and the CDOM source index (γ_0, index to trace source of CDOM as terrestrial or marine) for SEA waters. The relative contribution of these IOPs to light attenuation was investigated through diffuse attenuation of light (K_d) and euphotic depth (Z_d, the depth where the downwelling irradiance reaches 1% of its surface value), focusing on the role of CDOM and suspended sediments. Lastly, a vulnerability index is computed based on these IOPs together with K_d and Z_d to assess the locations in SEA at high risk of light limitation, i.e., where the photic zone compression is detrimental for the sustenance of planktonic and benthic communities. Our results will aid decision-makers in identifying the light vulnerable locations in the Sunda shelf sea that require adaptive management strategies in habitat conservation, fisheries management, and coastal and offshore planning.

Material and methods

IOCCG simulated dataset

We used the International Ocean Colour Coordinating Group (IOCCG) synthesized hydrolight simulated dataset containing IOPs and apparent optical properties for algorithm development, testing, and evaluation for satellite ocean color remote sensing in IOCCG Report 5 (IOCCG, 2006). It contains 500 sets of representative IOPs - phytoplankton absorption $a_{ph}(\lambda)$, CDOM absorption $a_g(\lambda)$, non-algal detrital absorption $a_d(\lambda)$, and particle backscattering coefficients $b_{bp}(\lambda)$ for 400-800 nm at 10nm interval along with corresponding $R_{rs}(\lambda)$ spectra and $K_d(\lambda$, depth=0, 10, 20, 30, 40 m) covering a large variety of open ocean to turbid coastal water types.

In situ Bio-optical data acquisition

Bio-optical and biogeochemical measurements were acquired at monthly to bi-monthly frequency from January 2019 to July 2020 as part of a biogeochemical time-series program at two offshore sites in the Singapore Strait (Figure 1): Kusu (1.226°N, 103.860°E) and Pulau Hantu (1.227°N, 103.747°E). Additional sites along the Johor Straits (separating Singapore from Malaysia to the north) and between Kusu and Hantu were sampled occasionally to cover different optical water types around Singapore. The *in situ* acquired dataset is referred to as the S.G. dataset from here on, and the IOCCG simulated dataset constitutes our validation dataset.

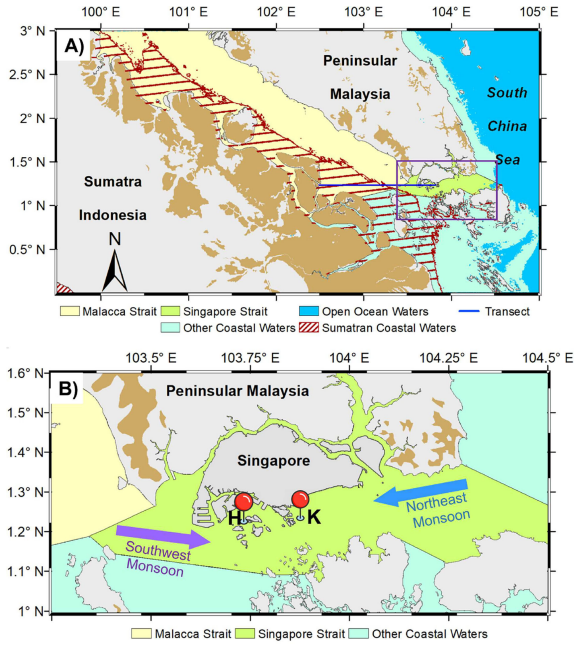

FIGURE 1
(A) Map of the study region showing the location of peatlands (brown in shading) and the delineation of water bodies across the Sunda shelf of Southeast Asia. The blue color line shows the transect from Sumatran coastal waters to Singapore Strait (latitude=1.24°CN. The purple box corresponds to the area shown in **(B)**. **(B)** The two main sampling sites in the Singapore strait waters are shown by red push pin indicators: the eastern site, Kusu (K) Kusu and western site Pulau Hantu (H). Purple and blue arrows show the mean current direction during each monsoon season.

Seasonal variation of coastal hydrodynamics is dominated by the bi-annual monsoon reversal in the region. The northeast monsoon (generally from December to early March) primarily brings north-easterly winds and heavy rain across the region during the first half of the northeast monsoon. The southwest monsoon exhibits south-westerly winds with relatively higher temperatures and less rainfall than the early northeast monsoon from June to September.

The sampling and analytical methods for CDOM and particulate absorption, backscattering coefficients, and radiometric measurements were summarized in (Martin et al., 2021) and (Zhou et al., 2021). Seawater samples were collected at 5m depth with Niskin bottles to analyze absorption by CDOM $a_g(\lambda)$ and DOC since October 2017. Briefly, samples were filtered on board through 0.2 µm pre-rinsed polyethersulfone filters and stored in amber borosilicate vials. Water (1L) for particulate absorption measurements was stored in HDPE bottles in the dark and filtered onto 25 mm diameter Whatman GF/F filters 3–6 hours later in the laboratory. Filters were flash-frozen and stored in liquid nitrogen. Particulate absorbance (sediment + phytoplankton) was measured from 300–800 nm with the filters held inside an integrating sphere on a PerkinElmer Lambda 950 spectrophotometer and corrected for pathlength amplification according to (Stramski et al., 2015). Samples were then depigmented to remove the chlorophyll-*a* absorption (phytoplankton) peak at 668 nm in dilute bleach for 15 min according to (Ferrari and Tassan, 1999), rinsed with ultrapure water, and remeasured. Phytoplankton absorption (a_{ph}) was calculated by subtracting the depigmented absorption spectrum (i.e., the non-algal particulate absorption, a_{dg}) from the total particulate absorption spectrum(a_p). CDOM absorption was measured on a Thermo Evolution300 spectrophotometer using 10-cm quartz cuvettes and ultrapure water as the reference.

Suspended sediment was collected directly from Kusu and Hantu reefs located in the Singapore Strait during the southwest monsoon (August 2018) using tube sediment traps deployed for one month (Morgan et al., 2020). The sediment mass collected was dried and weighed to determine the rate of sediment accumulation (g cm^{-2} d^{-1}). The grain size distribution of trap sediments was measured using laser diffraction analysis (Malvern Mastersizer 3000). The relative proportion of non-reef derived particles (i.e. clastic), total organic carbon (TOC), total inorganic carbon (TIC) in the bulk sediment mass was estimated using the loss-on-ignition (LOI) method (Heiri et al., 2001). X-ray powder diffraction (XRD) analysis (@FACTS, NTU, Singapore) was used to determine the mineralogical composition of representative suspended sediment from reef sites.

Volume scattering coefficient was measured at 124°C for 412, 440, 488, 510, 532, 595, 650, 676, and 715 nm using a Wetlabs BB9 at 1 m depth. Volume scattering coefficient was then converted to backscattering coefficients subtracting the absorption effects. The total absorption coefficient $a_t(\lambda)$ at 1-nm interval was measured using a TriOS OSCAR. The backscattering coefficient $b_b(\lambda)$ was converted to particulate backscattering by subtracting pure seawater contribution.

Hyperspectral (320 - 950 nm at 2 nm resolution) radiometric measurements were acquired using Trios-RAMSES radiometers. Downwelling irradiance, $E_d(0^+,\Lambda)$ and upwelling radiance $L_u(0^-,\Lambda)$ was measured in floating mode following the protocols suggested in (Fargion and Mueller, 2000) . Hence, the measurements were acquired during high sun elevation conditions (10 AM to 3 PM) under stable sun and sky conditions and were further used to compute the remote sensing reflectance $R_{rs}(\Lambda)$ (see Supplementary Information-1 Computation of Remote Sensing Reflectance).

Replicate radiometer measurements were acquired every 4 seconds on each measurement occasion. Only data corresponding to instrument inclination angles<5° was retained. Data were screened to remove outliers that differed by more than 2 S.D. from the mean R_{rs} and/or showed deviations in spectral shape. Replicate measurements that passed the quality checks were then used to recalculate the mean R_{rs}, which was then taken as the spectrum for that site. An overview of the S.G. *in situ* acquired IOPs (denoted at commonly used wavelength) and optically active constituents are tabulated in Table 1. In total, X=60 data points with concomitant measurements of all parameters, including R_{rs}, were collected.

Conceptual algorithm development

OLCI received (300 m resolution) above-water remote-sensing reflectance $R_{rs}(\Lambda,0^+)$ were processed by applying the algorithm proposed here. Estuarine, turbid coastal waters, and the open-ocean clear waters were first classified based on a) reflectance signature following (Lee et al., 2005) criteria $R_{rs}(670) \leq 0.0015$ sr^{-1} as open-ocean clear waters, b) reflectance ratio of $R_{rs}(665)/R_{rs}(443)$ similar to (Aurin et al., 2010) to distinguish highly turbid estuarine waters (ratio>0.35). Segregation criteria helped us select the appropriate algorithm to produce accurate IOP products for both open-ocean and turbid coastal waters. It is to be noted that (Shi and Wang, 2019) used $nL_w(745)$ based classification criteria for open ocean and coastal waters. However, their discrimination approach resulted in high data noise for moderate coastal turbid waters and did not blend our region's coastal and estuarine optical properties. Hence, we utilized two classification schemes ($R_{rs}(670)$ spectral signature and $R_{rs}(665)/R_{rs}(443)$ reflectance ratio) to determine which algorithm should be used for producing IOPs.

The band-integrated above-water remote-sensing reflectance $R_{rs}(\Lambda,0^+)$ from both datasets was then converted to underwater (just below the surface) remote sensing reflectance $r_{rs}(\Lambda, 0^-)$ following (Lee et al., 2002) as described in section 1 of Supplementary Information. $r_{rs}(\Lambda, 0^-)$ were processed using a

TABLE 1 Summary of in S.G. situ acquired IOPs and optically active constituents at Singapore Strait at standard wavelengths.

Parameters	Northeast monsoon Min-max (mean)	Southwest monsoon Min-max (mean)
$a_g(440\ nm)$ **(m^{-1})**	0.039-0.095 (0.065)	0.072-0.443 (0.224)
$a_d(440\ nm)$ **(m^{-1})**	0.035-0.20 (0.076)	0.015-0.21 (0.062)
$a_{ph}(440\ nm)$ **(m^{-1})**	0.039-0.084 (0.056)	0.038-0.077 (0.054)
$b_{bp}(550\ nm)$ **(m^{-1})**	0.016-0.064 (0.032)	0.012-0.076 (0.032)
DOC (µmol l^{-1})	70.39-81.03 (77.06)	65.53-103.81 (77.99)
TSM (mg m^{-3})	2.34-13.72 (6.72)	2.77-13.65 (6.64)
Chl-*a* (mg m^{-3})	0.44 -1.19 (0.75)	0.42-1.72 (0.92)
Temperature (°Cc)	28.15-29.28 (28.52)	29.48-31.32 (30.18)
Salinity	31.16-32.99 (31.76)	29.12-32.83 (31.25)
Turbidity (NTU)	0.73-2.26 (1.52)	0.01-3.68 (1.85)
Secchi disk depth (m)	2.2-3.7 (3.05)	2.0 -5.0 (3.32)

blended QAA algorithm (Shi and Wang, 2019) to estimate total absorption $a_t(\lambda)$ and backscattering coefficients $b_b(\lambda)$ as the next step of the algorithm development (see Supplementary Information Section 2). The adopted blended algorithm uses a near-infrared (NIR)-based quasi-analytical IOP derivation for turbid coastal/inland waters and Lee's quasi-analytical algorithm (QAA-v6) (IOCCG, 2006) for the open-ocean and less turbid coastal waters. Consequently, Lee's QAA-v6 (IOCCG, 2006) was used for open ocean ($R_{rs}(670) \leq 0.0015\ sr^{-1}$) and coastal waters ($R_{rs}(670) > 0.0015\ sr^{-1}$) with moderate turbidity whereas NIR-based QAA was applied for highly turbid estuarine waters (ratio>0.35) following the blended algorithm technique (Shi and Wang, 2019).

The performance of the algorithm for the simulated IOCCG and *in situ* S.G. dataset was evaluated individually (Supplementary Table S1) and as a combined-IOCCG+SG dataset (Figure 2). A high coefficient of determination (R^2, combined=0.99, S.G. = 0.99, IOCCG=0.99) signifies a strong correlation between the (Shi and Wang, 2019) defined NIR-based spectral slope η(779-865nm) and (IOCCG, 2006) defined visible spectral slope η(400-700nm). A lower value of root means square error, (RMSE, combined=0.09, S.G =0.09, IOCCG=0.09) in synergy with the slope values close to 1 (combined=1.048, S.G. = 0.981, IOCCG=1.07) indicates that the NIR-based spectral slope η(779-865nm) can be used to derive $b_{bp}(\lambda)$ in the visible bands for both the IOCCG and S.G. datasets. A high level of accuracy was observed between blended QAA derived $a_t(400)$ and counterparts (Figure 2B, Supplementary Table S1) from the validation dataset (combined R^2 = 0.99, S.G. R^2 = 0.99, IOCCG R^2 = 0.99) with a lower value of RMSE (combined=0.1 m^{-1}, S.G. = 0.03 m^{-1}, IOCCG=0.1m^{-1}) in synergy with the slope values close to 1 (combined=0.955, S.G. = 1.04, IOCCG=0.955). Similarly, high R^2 = 0.99 (combined), low RMSE ≤ 0.01 m^{-1}, and slope value of 0.86 for $b_{bp}(400nm)$ indicates that the algorithm is robust and can be used to derive IOPs for turbid waters (Figure 2C, Supplementary Table S1). However, as the combined dataset is overwhelmed by the IOCCG data (N=500), the combined statistical relations and fits follow the IOCCG simulated data. Following (Shi and Wang, 2019), $a_t(\lambda)$ is then decoupled into a_{ph}

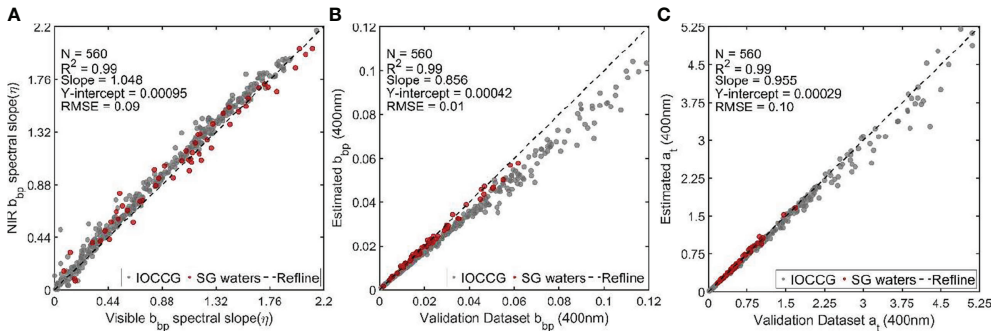

FIGURE 2
Comparison of **(A)** spectral slope of particulate backscattering η computed using visible bands (400-700 nm) and NIR bands (779-865). **(B)** blended QAA derived and IOCCG+SG quantified $b_{bp}(400nm)$. **(C)** blended QAA derived IOCCG+SG quantified a_t (400nm) for Sentinel OLCI spectral bands.

(λ) and $a_{dg}(\lambda)$ according to Lee's QAA algorithm (Lee et al., 2005) with the empirical approach relating $a_t(\lambda)$, and $r_{rs}(\lambda)$ at the blue and green bands (see Supplementary Information 3- Decoupling total absorption at(λ) according to Lee's QAA).

High-quality IOP products can be obtained with the blended QAA for all water types (Shi and Wang, 2019). We extended this algorithm to further decouple $a_{dg}(\lambda)$ to absorption by CDOM, $a_g(\lambda)$, and by non-algal detritus particles, $a_d(\lambda)$, using the area-under-the-curve method. The enclosed area under the a_{dg} spectral curve is highly correlated with the spectral shape of $a_g(\lambda)$ and $a_d(\lambda)$ (Chen et al., 2017). The normalized area over reflectance curve (NAOC) index initially developed by (Delegido et al., 2010) is a commonly used spectral index for the chlorophyll-*a* mapping of heterogeneous cropping areas (Delegido et al., 2011; Carmona et al., 2017). Following a similar concept, (Chen et al., 2017) correlated variations in $a_{dg}(443)$ with the triangular area under the reflectance curve for $a_g(443)$ retrievals. We adopted the same concept and calculated the area under the a_{dg} spectral curve between wavelengths 400 and 443 nm and 412 and 443 nm using the trapezoidal numerical integration approach and correlated with $a_g(400)$ and $a_g(412)$.

$$area_a dg(\lambda_1, \lambda_2) = \int_1^2 a_{dg}() \tag{1}$$

CDOM - absorbs more strongly in short-wavelength light ranging from ultraviolet to blue. The shortest wavelength band lies around 400 nm in current ocean color sensors and hence is used for CDOM derivation here. The combined IOCCG+SG dataset present (Figures 3A, B) a strong correlation (linear correlation, r≥0.96, pval=0, and R^2≥0.93) between the area under the a_{dg} spectral curve and $a_g(\lambda)$ for 400 and 412 nm. Remotely sensed $a_g(400)$ and $a_g(412)$ was computed using the observed relation (Supplementary Table S1) between area under the a_{dg} spectral curve and $a_g(\Lambda)$ obtained from combined dataset

$$a_g(400) = area\_a_{dg}(400, 443) * 0.088 \tag{2}$$

$$a_g(412) = area\_a_{dg}(412, 443) * 0.122 \tag{3}$$

Close distribution along the 1:1 reference line in Figure 3C, D with high strength of regression signifies less scatter between blended QAA estimated $a_g(\lambda)$ and its counterparts from the validation dataset for 400nm (combined R^2 = 0.95, S.G. R^2 = 0.94, IOCCG R^2 = 0.95) and 412nm (combined R^2 = 0.93, S.G. R^2 = 0.94, IOCCG R^2 = 0.94). The linear correlation coefficient, r≥0.96 and RMSE ≤ 0.07 m^{-1}, is indicative of a high correlation. The statistical evaluations (Supplementary Table S1) give us the confidence that the area under the a_{dg} spectral curve can be used to estimate $a_g(\lambda)$ for 400 and 412 nm. This proves that the proposed algorithm delivers satisfactory results with both the simulated and the S.G. *in situ* datasets when a more diverse set of samples are available.

The spectral slope of CDOM (S_g) was determined by fitting a_g between 400 and 412 nm to an exponential model.

$$a_g(\lambda) = a_g(400)e^{-S_g(\lambda-400)} \tag{4}$$

CDOM source index (γ_0) was calculated from absorption for dissolved organic matter $a_g(\lambda)$ (Shanmugam, 2011) to distinguish between CDOM of terrestrial origin and CDOM produced autochthonously in the marine environment

$$\gamma_0 = \frac{a_{cdom}(350nm) - \left(\frac{1}{\gamma}\right)}{a_{cdom}(350nm) + \left(\frac{1}{\gamma}\right)} \tag{5}$$

The γ was obtained by fitting the CDOM absorption spectrum between 350–650 nm to a hyperbolic equation (Shanmugam, 2011)

$$a_{cdom}(\lambda) = a_{cdom}(350nm)\left(\frac{\lambda}{350}\right)^{-\gamma} \tag{6}$$

(Shanmugam, 2011) used a formulation of equation 5 that causes a sign reversal, such that terrigenous CDOM is characterized by negative values and marine CDOM by positive values; we formulated the equation such that terrigenous CDOM has positive values and marine CDOM has negative values, as in the original publication. The diffuse attenuation coefficient (K_d) for downwelling irradiance (E_d) is an essential parameter for accurate estimation of the light distribution at depth (z) in ocean optics and is defined as

$$K_d(z) = \frac{-1}{E_d(z)}\frac{dE_d(z)}{dz} \tag{7}$$

Several semi-analytical algorithms for K_d retrieval have been developed based on the relationship between total absorption (at) and backscattering (b_b) coefficients to light attenuation (Gordon et al., 1975; Kirk, 1984; Lee et al., 2005; Lee et al., 2014). Radiometer measured and semi-analytically calculated K_d and Z_d -10% (Lee et al., 2005) for this region were compared by (Martin et al., 2021) with a mean absolute percent error for euphotic zone depth of 9%. Hence, we adopted the same approach for K_d retrieval developed by (Lee et al., 2014) to account for a shift in the phase function between pure water molecular backscattering and particle backscattering.

$$K_d(z, \lambda) = (1 + m_0 0) * a_t(\lambda) + (1 -_w (\lambda)) * m_1 * \left(1 - m_2 * e^{-m_3 * a_t(\lambda)}\right) * b_b(\lambda) \tag{8}$$

Where γ and $m_{0\text{-}3}$ are spectral constants and do not vary with water properties and θ_0 is the solar zenith angle (degrees), and $\eta_w(\Lambda)$ is defined as

$$_w(\lambda) = \frac{b_{bw}(\lambda)}{b_b(\lambda)} \tag{9}$$

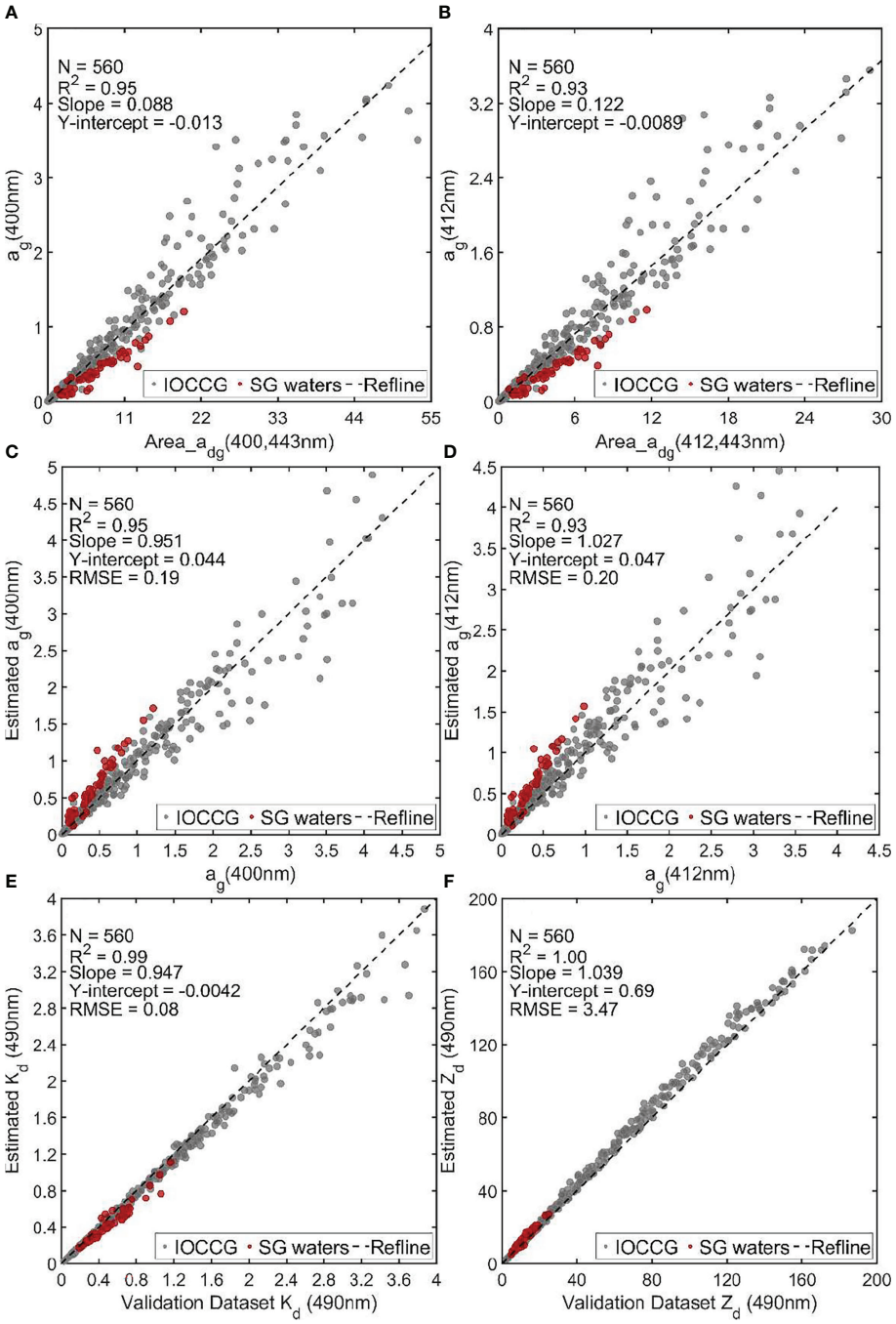

FIGURE 3
Comparison plots of **(A)** area under the a_{dg} spectral curve and a_g(400nm). **(B)** area under the a_{dg} spectral curve and a_g(412nm). **(C)** IOCCG+SG quantified and area-based estimations of a_g(400nm). **(D)** IOCCG+SG quantified and area-based estimations of a_g(412nm). **(E)** K_d (490) derived from IOPs using blended QAA and IOCCG+SG. **(F)** Z_d(490nm) derived from IOPs using blended QAA and IOCCG+SG.

Spectral attenuation budgets were calculated as the fractional contribution of total absorption and backscattering to K_d at each band (equation 8). Similarly, spectral absorption budgets were calculated as the fractional contribution of each constituent (CDOM, non-algal detritus particles, phytoplankton, and water) to the total absorption at each band.

The penetration depth Z_d at 490nm where downwelling irradiance E_d (490, z) reaches 1% of E_d(490,0−) is computed as follows

$$Z_d(490) = -\frac{\log_e(10^{-2})}{K_d(490)} \quad (10)$$

Figures 3E, F shows the performance of the $K_d(490)$ and $Z_d(490)$ derived from IOPs using blended QAA compared to the $K_d(490)$ and $Z_d(490)$ derived using the IOCCG+SG dataset. High-quality retrievals of IOP products led to a strong correlation and less scatter between the K_d estimated using blended QAA and IOCCG+SG dataset with R^2 = 0.99 and RMSE=0.08 m^{-1}. Overall, the statistical evaluation shows close agreement between the blended QAA and derived IOPs with high correlation coefficients, low RMSE, small offsets, and slope values ~1, reinforcing that the proposed algorithm is robust and stable enough for IOP retrievals.

IOP based vulnerability index of photic zone compression

Insufficient light from the surface to the benthos can cause the negative impacts on marine ecosystems. Mathematically, vulnerability is the *likelihood* of low-light conditions in water times the *amount* of attenuation. Overall vulnerability ranks were calculated in a four-step process:

i. The number of controlling factors or key risk sources that influence the penetration of light,
ii. The associated impact or the response of an aquatic system using a 0-1 loss function to the controlling factors,
iii. The frequency and duration of occurrence of these controlling factors to understand the current state of the aquatic system, and
iv. A potential probability of occurrence of low-light conditions.
v. The number of controlling factors (N_x) considered here are a) total absorption coefficient $a_t(490nm)$, b) backscattering coefficient $b_b(490nm)$, c) diffuse attenuation coefficient, $K_d(490nm)$, and d) penetration depth, $Z_d(490nm)$. The impact of each of these controlling factors (x) can be associated with 0–1 loss function

$$l(x, x_{th}) = \begin{cases} 0, & x < x_{th} \\ 1, & x \geq x_{th} \end{cases} \quad (11)$$

The loss function implies that the light attenuation is manageable and the loss function, l=0, when a controlling factor is within the threshold value ($<x_{th}$), otherwise the light traveling through an aquatic body loses its power and intensity over a small distance. A loss function (0–1) corresponding to each of these controlling factors will aid in determining the likelihood (not likely and very likely) of light attenuation in the water column. Thresholds for the controlling factors, $a_t(\lambda) \geq 1 m^{-1}$ and $b_b(\lambda) \geq 0.5\ m^{-1}$, defined here are based on the analysis of the results obtained by our Singapore Strait data and referring to the maximum values from tropical coastal turbid waters (Oubelkheir et al., 2006; Ambarwulan et al., 2010; Bowers et al., 2011; Cherukuru et al., 2020) and turbid coastal waters elsewhere (Babin, 2003; Doxaran et al., 2006). The isolume depth where the PAR reaches 0.415 mol photons m^{-2} day^{-1}, below which light is insufficient to support photosynthesis, has been regarded as a useful threshold for the euphotic depth (Boss and Behrenfeld, 2010; Thushara et al., 2019). The estimated isolume depth based on the PAR values measured by (Morgan et al., 2020) for Kusu and Pulau Hantu is 16.26 ± 3.8m and 15.05 ± 3.25m, respectively. As the vertically compressed coral depth distributions have been reported in these waters (Morgan et al., 2020), the minima of the isolume depth observed in these were used as a basis for setting the threshold depth ($Z_d \leq 12m$) for the SEA waters. Consequently, a high value of the loss function indicates the rapid absorption ($a_t(\lambda) \geq 1 m^{-1}$) or scattering ($b_b(\lambda) \geq 0.5\ m^{-1}$) of light responsible for elevated attenuation ($K_d \geq 0.5\ m^{-1}$ and limiting the depth of penetration, Z_d to ≤15m beyond which light is insufficient to support photosynthesis.

With the insight that the vulnerability of the aquatic medium also depends on the duration (number of days) for which light availability was limited, the duration function associated with the loss of light is defined as

$$D(x, x_{th}; d, d_{th}) = \begin{cases} 0, & x < x_{th} \\ 1, & x \geq x_{th} \quad and \quad d > 0, d_{th} = 0 \end{cases} \quad (12)$$

For the annual vulnerability index, d represents the total number of days in a year for which $x \geq x_{th}$. Based on equation 12, the final vulnerability index (Supplementary Flowchart F1) for the above-mentioned four factors controlling the attenuation of light was calculated as

$$V(l(x, x_{th}); D(x, x_{th}; d, d_{th})) = \frac{1}{N_x} \sum_{n=1}^{n=N_x=4} \pi(l(x, x_{th}); D(x, x_{th}; d, 0)) \quad (13)$$

Where represents the vulnerability associated with each controlling factor and defined as:

$$\pi(l(x, x_{th}); D(x, x_{th}; d, 0)) = l(x, x_{th}) \frac{\sum_{d>0} D(x, x_{th}; d, 0)}{\sum_{d>0} D(x, 0; d, 0)} \quad (14)$$

The vulnerability index will rank the order of risk (Not vulnerable: 0-0.2, Low: 0.2-0.4, Moderate: 0.4-0.6, High: 0.6-0.8, and critically high >0.8) to low-light conditions in the aquatic

body. Thus, a high vulnerability indicates elevated losses of light persisting for a longer duration, resulting in low-light conditions in the aquatic body. Vulnerability assessment will aid in identifying locations threatened by poor underwater light levels too weak to allow photosynthesis to occur.

Results

Spatial variation of IOPs and diffuse attenuation coefficient

The four-year average spatial distribution map (Figure 4) displays relatively low values of a_t(400nm) and a_g(400nm) for the offshore marine waters. Conversely, high concentrations of a_t (400nm) >0.7m^{-1} and a_g(400nm) >0.5m^{-1} are observed for the coastal waters, especially through the Sumatran coastal water belt adjacent to the river mouths draining into the Malacca Strait. The CDOM source index γ_0 was observed in the range of >0.6, indicating a terrigenous source of CDOM near the Indonesian river mouths. In contrast, low negative values in the clear offshore waters of the South China Sea indicate an autochthonous marine source of CDOM. Intermediate values of γ_0 ranging from 0-0.6 result from the mixing of terrestrial and marine CDOM sources. Variation in the particulate backscattering coefficient b_{bp}(400nm) is observed in response to changing sediment concentrations, with lower values in clear marine waters (<0.25 m^{-1}) and higher values (≥0.5m^{-1}) in turbid sediment-rich coastal areas receiving a significant amount of freshwater input from rivers (Figure 4). Extensive CDOM and sediment-rich plumes around the coastal water belt promoted intense attenuation of light, with K_d(490)≥1.5 m^{-1} and shallow underwater light penetration, Z_d(490)<5m (Figure 4). This implies that light intensity will be reduced by one natural log within 1.5m of water, thereby limiting the depth of light penetration to 5m. Within the Singapore Strait, a_t (400nm) values ranged between 0.4-1.5 m^{-1}accompanied by CDOM a_g(400nm) between 0.4-1.0 m^{-1} and the CDOM source index γ_0 >0.6,. K_d(490) ranged the lowest value of 0.5m^{-1} to a peak value of 0.75m^{-1}, thereby reducing the penetration depth, Z_d(490) from<15m to<10m in the Singapore Strait waters.

Monsoon-driven seasonal variation of CDOM rich waters

The South China Sea water is steered along the east coast of the Malay Peninsula during the northeast monsoon. It then diverts into the Singapore Strait (Gordon, 2005; Gordon et al., 2012), carrying only moderate amounts of a_g(400nm) within the range of 0.2-0.5 m^{-1} in synergy with intermediate values of CDOM source index, γ_0 falling between 0-0.5 (Figure 5, Supplementary Figures S3–S4). Mixing of terrestrial and

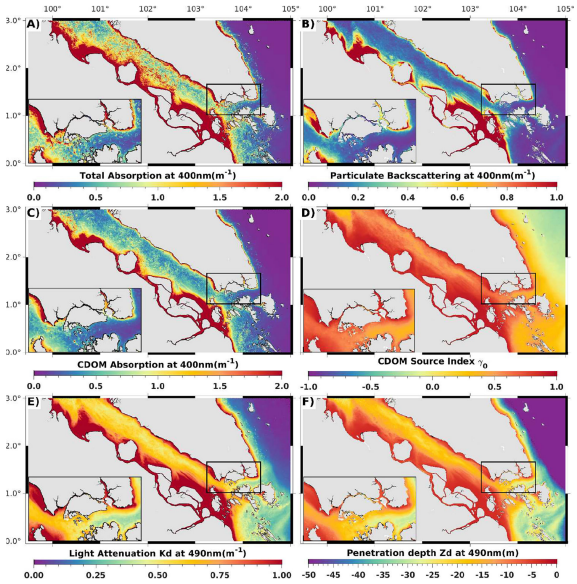

FIGURE 4
Spatial distribution of the 2017–2020 mean values of blended QAA derived optical properties **(A)** Total absorption coefficient of light (a_t) at 400 nm. **(B)** Particulate backscattering (b_{bp}) at 400nm. **(C)** CDOM absorption coefficient (a_g) at 400 nm. **(D)** CDOM source index, γ_0 (values ≥0.5 indicate the increasing dominance of terrigenous origin of CDOM over marine) **(E)** Diffuse attenuation coefficient of light (K_d) at 490 nm. **(F)** Depth of penetration of light at 490 nm (Z_d, 1% of the surface value). The black box corresponding to the Singapore Strait area is shown in the left corner of each image.

marine sediments resulted in b_{bp}(400nm) between 0.2-0.5 m^{-1}, K_d (490)>0.1 m^{-1}, and Z_d(490)≤15m (Figure 5 and Supplementary Figures S1–S4). Slight fluctuations in CDOM absorption and sediment backscattering were observed during the drier late northeast and inter-monsoon months (February-March and October-November). The Singapore Strait receives a mix of waters corresponding to CDOM source index γ_0 >0.7 (Figure 5, Supplementary Figures S3, S4) from the Java Sea in the south and the Sumatran coastal waters entering through Malacca Strait (Gordon, 2005; Gordon et al., 2012) during the southwest monsoon. The transport of organic matter rich (a_g(400nm): 1.0-2.0 m^{-1}) and sediment-laden (b_{bp}(400nm): 0.5-2.0 m^{-1}) waters from the Sumatran coast to the Singapore Strait was detected during this season (Figure 6). The region experiences a turbulent mixing of the water column and resuspension of sediments, which consequently would explain the higher values of b_{bp} (400nm) >0.5m^{-1} with a wider stretched distribution of K_d (490) >0.75, thereby reducing the depth of light penetration Z_d to<10m (Figures 5, 6, Supplementary Figures S2, S6, S7). It is apparent from our satellite observations that the light attenuation represented by K_d(490) is year-round (in all the seasons) high along the Sumatran coastal waters (Figure 5, Supplementary Figure S6), with values >1.5 m^{-1} constraining the depth Z_d(490)<5m throughout the year. In comparison, significant seasonal heterogeneity was observed in the Malacca Strait, with K_d fluctuating between ≤0.75 to >1.5 and Z_d between ≤10 m to<5m (Figure 5, Supplementary Figures S6, S7).

Quality of underwater light

Seasonal inputs of CDOM and sediment contribute to substantial variation in the light attenuation budget. The relative contributions of total absorption (a_t) to K_d at 490 nm varied from 66% in northeast monsoon to 61% in the southwest monsoon, along with significant contribution from the backscattering (b_b) of 34% in northeast monsoon to 39% in southwest monsoon for Singapore Strait and Malacca Strait waters (Figure 7). The contributions of a_t reduced from ~61% to 56% from northeast monsoon to southwest monsoon for Sumatran coastal waters, thereby increasing the b_b contributions from 39% to 44% (Figure 7). CDOM generally dominated the absorption budget in all seasons across all the coastal waters (~45% of total absorption) but to a greater extent in the southwest monsoon. The CDOM domination to the total attenuation (absorption+backscattering) budget was ~22% for Singapore Strait waters and ~30% for Sumatran coastal waters during the northeast monsoon, which increased to ~27% and ~36%, respectively, during the southwest monsoon (Figure 7). Conversely, absorption by detritus remained smaller (≤10%) than phytoplankton absorption (~20%) in all seasons for Singapore Strait waters. Contrastingly, absorption by detritus was higher (~20%) than phytoplankton absorption (≤10%) for Sumatran coastal waters (Figure 7).

The peak wavelength corresponding to minimum K_d and at a maximum penetration depth (Figures 8A, B) demonstrates a spectral shift in the underwater light field. Blue wavelengths penetrate the deepest (≥40m) in offshore waters of the South China Sea. Malacca Strait and Singapore Strait waters shift the underwater light to ~560nm wavelengths during inter-monsoons and the northeast Monsoon (Figures 8A, B). The underwater light spectrum is further shifted to longer wavelengths ≥620nm for the southern part of Malacca Strait and eastern Singapore Strait during the southwest monsoon. Similarly, the Sumatran coastal waters displayed a spectral shift to even longer red wavelengths >620nm during the southwest monsoon (Figures 8A, B).

The significant seasonal variations in absorption and scattering by optically active constituents caused the seasonal fluctuations in the sensitivity of the Southeast Asian water to possible threats of photic zone compression for planktonic and benthic primary productivity (Figure 9 and Supplementary Figure S7). The joint probability evaluations of intensity and duration of the four controlling factors ($a_t(\lambda)$, $b_b(\lambda)$, K_d, Z_d) indicates that the clear marine waters are not vulnerable to light as a liming factor in any season having a vulnerability index (VI) ≤0.2. Similarly, the central part of the Malacca Strait and central to western Singapore Strait remains not vulnerable to light as a limiting factor (VI ≤ 0.2, Figure 9) for most of the months. The rest of the waters have been assigned to different vulnerability categories spanned from Low to critically High. A medium (VI=0.4-0.6, Figure 9) to high range (VI=0.6-0.8, Figure 9) of vulnerability is detected in most of the coastal waters of the Malacca Strait and eastern Singapore Strait during inter-monsoons and the northeast Monsoon (Supplementary Figure S7). However, the southern part of Malacca Strait is identified as having a high range of vulnerability (VI=0.6-0.8, Figure 9). Further, a critically high state of vulnerability (VI≥0.8, Supplementary Figure S7) is realized in the southern part of Malacca Strait during the southwest monsoon extending further towards the eastern Singapore Strait waters, which acquires a high range of vulnerability (VI=0.6-0.8, Figure 9) during the season and a medium to high vulnerability status (VI=0.6-0.8, Supplementary Figure S7) is realized by the central part of the Malacca Strait during the southwest monsoon. The Sumatran coastal water belt delineated in Figure 1 is categorized as critically vulnerable (VI>0.8, Figure 9) to light as a limiting factor year-round (in all the seasons) (Supplementary Figure S7).

Discussion

We extended the blended QAA for the derivation of CDOM absorption coefficient along with other IOPs from satellite observations. Blended QAA has been demonstrated to

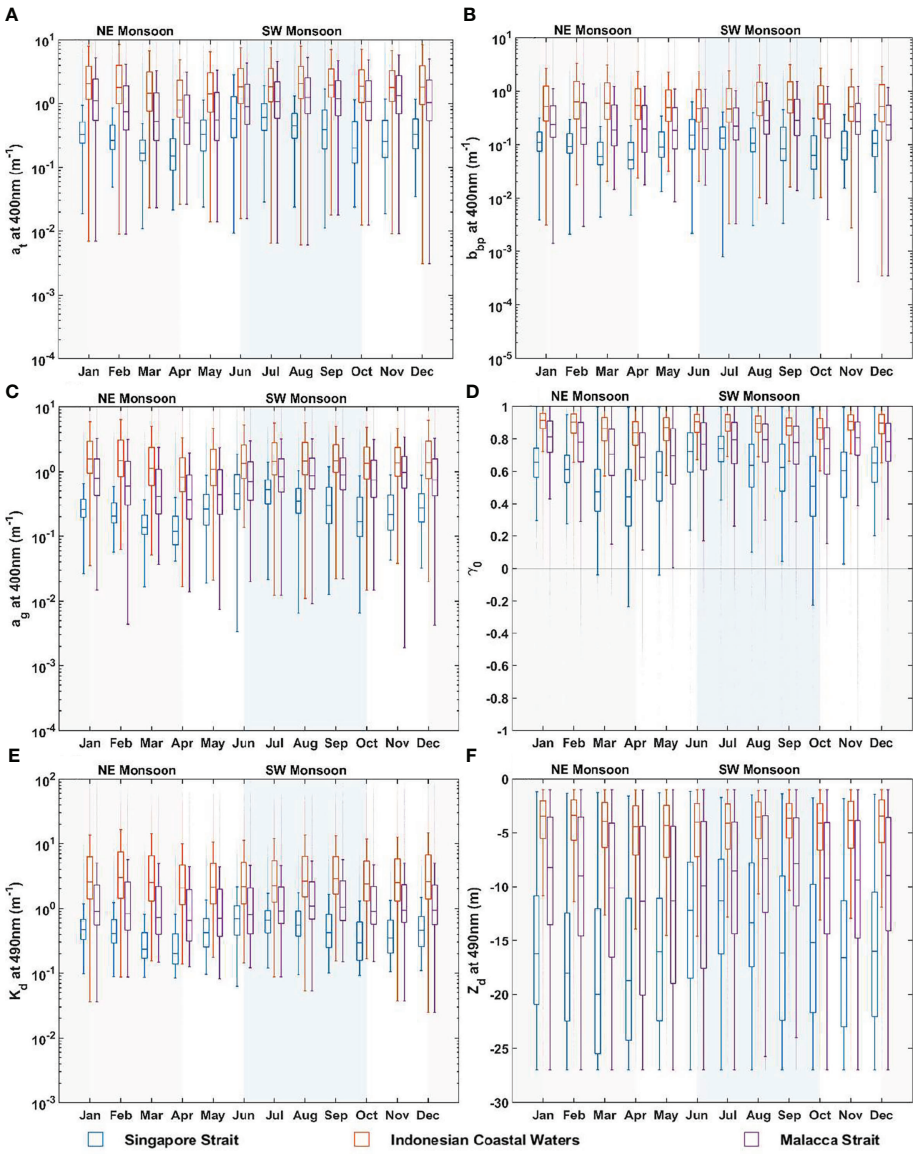

FIGURE 5
Box plots of monthly mean (2017-2020) values of bio-optical parameters across Singapore Strait, Malacca Strait, and Sumatran Coastal waters defined in Figure 1. Bio-optical parameters derived from Sentinel OLCI were **(A)** Total absorption coefficient of light (a_t) at 400 nm. **(B)** Particulate backscattering (b_{bp}) at 400nm. **(C)** CDOM absorption coefficient (a_g) at 400 nm. **(D)** CDOM source index, γ_0 (values $\geq$0.5 indicate the increasing dominance of terrigenous CDOM over CDOM of marine origin). **(E)** Diffuse attenuation coefficient of light (K_d) at 490 nm. **(F)** Depth of maximum penetration of light at 490 nm (Z_d, 1% of the surface value). Box plot for the offshore marine waters is avoided here due to relatively lower and stable values of all the parameters.

generate accurate and robust $b_{bp}(\lambda)$ and $a_t(\Lambda)$ retrievals for a wide range of coastal waters such as the Bohai Sea and the Yellow Sea in China's east coastal region, Amazon River Estuary, and Mississippi River Estuary and tributaries (Shi and Wang, 2019). The area under the spectral curve technique for deriving a_g has been demonstrated for Taihu Lake (Chen et al., 2017). In addition, the area delimited by the reflectance curve retrieved from satellite measurements has been widely used as a proxy for chlorophyll-*a* concentration (Gitelson, 2005; Chen et al., 2011; Hu et al., 2012). Hence, we implemented the proposed algorithm for peatland-influenced and CDOM-rich Southeast Asian coastal waters. The advantageous feature of this algorithm is that it can be easily adopted for the application over CDOM-dominated waters in other regions of the world. In addition, the straightforward vulnerability assessment technique can be easily adopted for application over turbid waters for underwater light

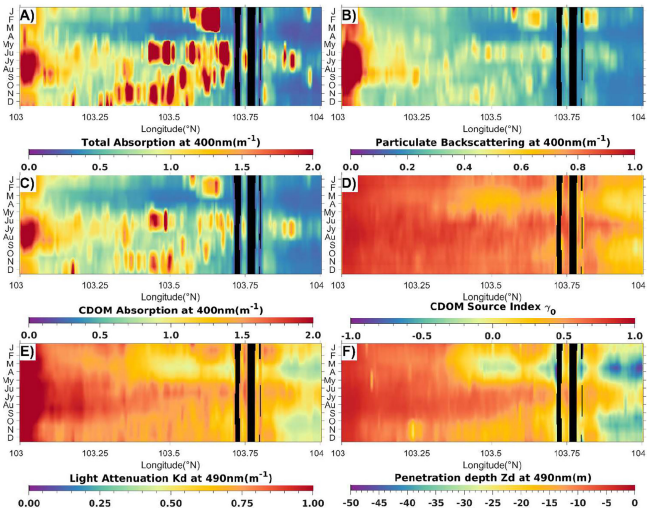

FIGURE 6
Transect from Sumatran coastal waters to Singapore Strait (latitude=1.24°CN) for monthly averaged (2017-2020) optical properties **(A)** Total absorption coefficient of light (a_t) at 400 nm. **(B)** Particulate backscattering (b_{bp}) at 400nm. **(C)** CDOM absorption coefficient (a_g) at 400 nm. **(D)** CDOM source index, γ_0. **(E)** Diffuse attenuation coefficient of light (K_d) at 490 nm. **(F)** Depth of maximum penetration of light at 490 nm (Z_d, 1% of the surface value). The figure displays the transport of organic matter rich and sediment-laden waters from the Sumatran coast to Singapore Strait during the Southwest monsoon (June-September).

sensitivity evaluations irrespective of any algorithm utilised for derivation of CDOM or sediment concentration.

Sources of organic matter-rich and sediment-laden waters

Overwhelmingly high values of a_g(400nm), representing CDOM concentrations and b_{bp}(400nm), representing suspended sediment concentrations observed throughout the Sumatran coastal waters (Figure 4) attest to the extensive influence of continental inputs from riverine discharges in the estuarine and coastal environments. The spectral slope of CDOM (S_g) is often considered to be an indicator of the source of CDOM (Kirk, 1994; Cherukuru et al., 2020), with values ≥0.021 nm^{-1} associated with marine sources and ≤0.014 nm^{-1} indicating terrestrial sources. However, an advanced indicator based on the spectral characteristics - the CDOM source index, γ_0 - was observed to be ≥0.75 year-round for Sumatran coastal waters (Figures 4–5 and Supplementary Figure S4). The source index γ_0 was compared with the known markers (spectral slope from 275–295 nm, $S_{275\text{-}295}$ and the spectral slope ratio S.R., the ratio of the 275–295 nm slope to the 350–400 nm slope) of terrestrial DOC for Southeast Asian waters by (Sanwlani et al., 2022). And the source index γ_0 was observed to be an appropriate tracer for terrigenous CDOM in remote sensing analyses and by inference of DOC in these waters. Indonesia harbors extensive tropical peatlands (Page et al., 2011; Dommain et al., 2014), and the large supply of dissolved organic matter from Sumatra have been reported to influence the CDOM and the carbonate system in the Sunda Shelf Sea (Wit et al., 2018; Zhou et al., 2021). The peatland-draining rivers in Southeast Asia are characterized by high CDOM and DOC, with a_g(350nm) of 50–200 m^{-1}, and >1000 µmol DOC l^{-1} (Alkhatib et al., 2007; Rixen et al., 2008; Moore et al., 2011; Wit et al., 2015; Martin et al., 2018; Wit et al., 2018), which are among the highest values found in rivers globally. Interestingly, these peat-draining rivers oxidize only a minor amount of organic carbon to CO_2 relative to the high DOC concentrations (Müller-Dum et al., 2019). Consequently, increases in peat draining riverine flux to coastal waters effectively increase the terrigenous organic matter flux. Moreover, CDOM in estuaries and shelf seas demonstrates conservative mixing across the salinity gradients (Fichot and Benner, 2012; Martin et al., 2018; Martin et al., 2021), promoting the regional advection of CDOM to far across shelf seas. Strong on-shore (Sumatran) to offshore (Malacca Strait) gradients in CDOM (Figure 4 and Supplementary Figure S3) show the freshwater mixing of organic-rich Sumatran with marine waters in the Malacca Strait.

While the monsoon-driven rainfall variation directs the CDOM and DOC flux from tropical peatlands to Sumatran coastal waters (Rixen et al., 2016), the regional advection and mixing of peatland-derived coastal waters drive the CDOM heterogeneity (Figures 5, 6) in Singapore Strait waters. The Singapore Strait is located in the central Sunda Shelf Sea and

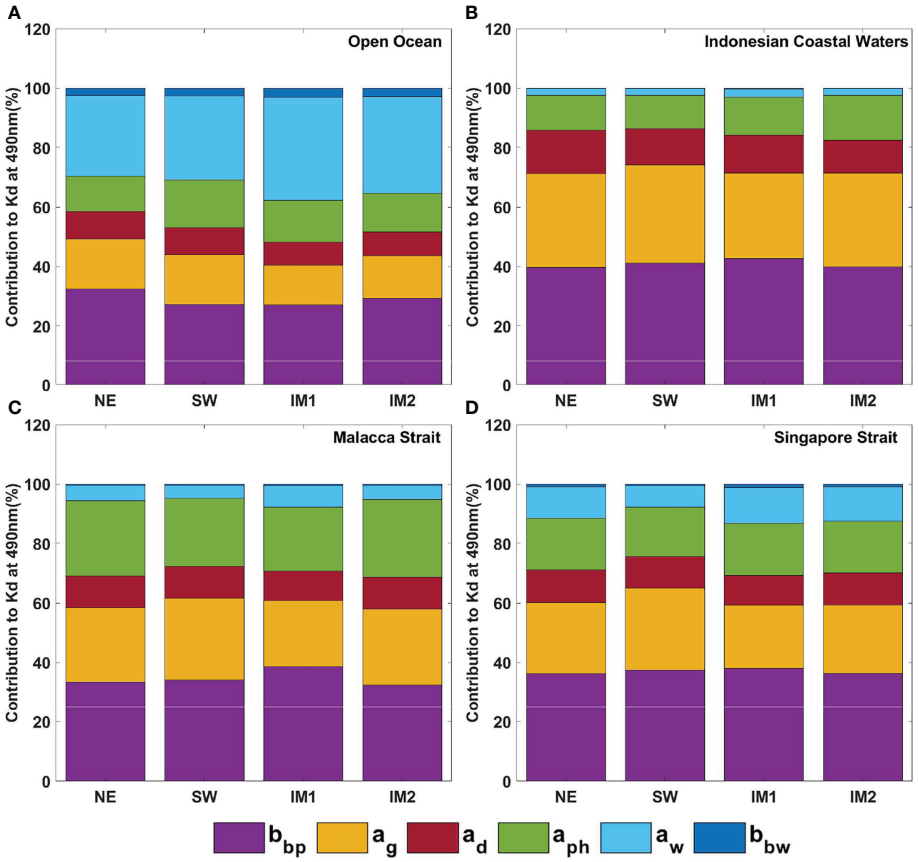

FIGURE 7
Relative contribution of bio-optical components to diffuse attenuation coefficient of light (K_d) at 490 for **(A)** Open Ocean waters, **(B)** Indonesian coastal waters, **(C)** Malacca Strait, and **(D)** Singapore Strait defined in Figure 1. Relative contribution is computed seasonally for absorption coefficient of water (a_w) at 400 nm, CDOM absorption coefficient (a_g) at 400 nm, detritus absorption coefficient (a_d) at 400 nm, phytoplankton absorption coefficient (a_{ph}) at 400 nm, particulate backscattering (b_{bp}) at 400nm, and backscattering by water (b_{bw}) at 400nm.

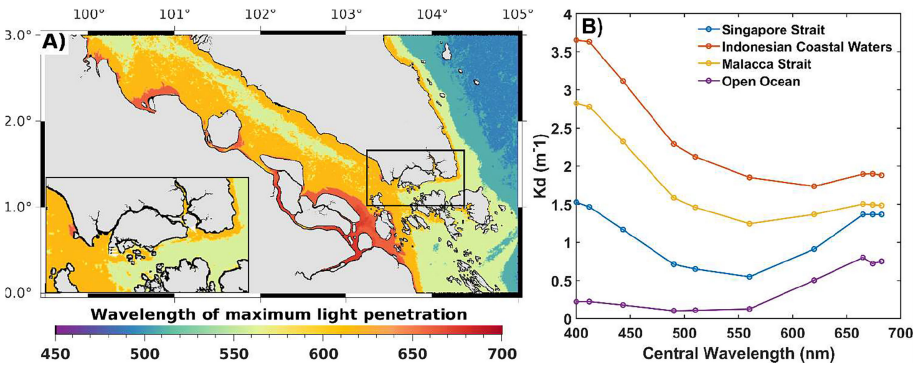

FIGURE 8
Spectral quality of light in the water column. **(A)** Spatial distribution of the mean value (2017–2020) of the central wavelength at maximum penetration of light. **(B)** Spectral distribution of light across Singapore Strait, Malacca Strait, Open Ocean, and Sumatran Coastal waters.

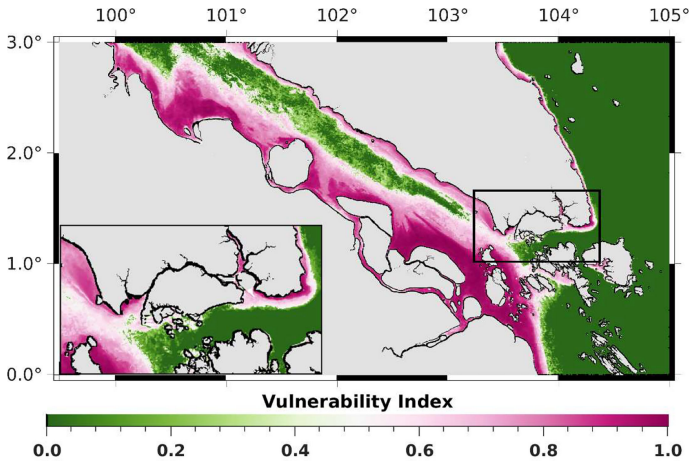

FIGURE 9
Sentinel-OLCI derived mean (2017-2020) distribution of vulnerability index of photic zone compression across Sunda shelf waters.

close to coastal peatlands on Sumatra. The difference in the sea level between the east and west sides of Singapore Strait fluctuates over 40 cm annually, with the lowest levels in June–July and a peak in November (Wyrtki, 1961; van Maren and Gerritsen, 2012). This creates a hydrodynamic pressure gradient between the Strait's eastern and western sides and drives the water to flow from east to west through the Strait with velocities of 10–15 cms^{-1} for the period of the northeast monsoon. The gradient reverses during the southwest monsoon, resulting in a persistent easterly flow (Wyrtki, 1961; van Maren and Gerritsen, 2012). This is the period when the Singapore Strait receives waters from the Java Sea in the south and mixes with the Sumatran peatland-influenced waters entering through Malacca Strait. The correlated seasonal variations of CDOM absorption, particulate backscattering, spectral characteristics in the form of CDOM source index (Figure 5 and Supplementary Figures S1–S4), accompanied with Indonesia to Singapore transect (Figure 6), all indicate the advection of organic-rich ($a_g(400nm)>1.0m^{-1}$) and sediment-laden ($b_{bp}(400nm)>0.5m^{-1}$) waters that originate from Sumatra's peat-draining rivers to the Singapore Strait. These observations demonstrate that Sumatran peatlands are the most significant source of the terrigenous CDOM ($\gamma_0>0.6$) that govern the biogeochemical processes in the central part of the Sunda shelf. This observation is consistent with (Siegel et al., 2019), who demonstrated that CDOM spreads out from Sumatra into the Malacca and Karimata Straits. Consequently, advection-driven amplification (5-fold increase) in CDOM and sediment concentrations in Singapore Strait (Figures 5, 6) are evident during the southwest monsoon relative to the inter-monsoon periods. The observation of 5 to 10-fold seasonal variation in light absorption by CDOM is also reported by (Martin et al., 2021) and (Zhou et al., 2021). However, much smaller amounts of terrestrial influx reach the Singapore Strait during the northeast Monsoon when more clearer marine water is conveyed from the South China Sea to Singapore Strait. The Malay Peninsula only harbors few areas of peatland (Dommain et al., 2014). Consequently, a minor contribution of CDOM and sediment concentrations was observed along the east coast of the Malay Peninsula.

In contrast to the strong seasonality of CDOM and sediments, there was no clear seasonal pattern to absorption by phytoplankton. Generally, absorption by photosynthetic pigments represents a more dominant optical component in light attenuation. However, the relatively low concentrations of chlorophyll-*a* signify consistently lower absorption by phytoplankton along the Sumatran coast, which further reinforces that the production of autochthonous, marine CDOM is unlikely to be a dominant source of organic matter. Moreover, terrestrial CDOM is enriched in humic and aromatic compounds compared to algal-derived CDOM, which is composed more of protein-like and aliphatic material and contains fewer colored components (Harvey et al., 1983; Massicotte and Frenette, 2011). This property is reflected in the spectral profile of CDOM (Helms et al., 2008; Oestreich et al., 2016) and captured in the CDOM source index (Shanmugam, 2011) computed here ($\gamma_0>0.6$), which further reinforces our conclusion that peatland-derived allochthonous material dominates the CDOM pool in this region.

Previous studies on the low biodegradability of dissolved organic matter from Southeast Asian peat-draining rivers suggest that photodegradation is the controlling process altering the CDOM pool in Sunda shelf waters (Nichols and Martin, 2021). The elevated CDOM absorption $a_g(400nm)$ in synergy with high particulate backscattering (b_{bp}) during the northeast monsoon reflects lower photodegradation rates due to insufficient sunlight and greater cloud cover in the entire region.

Terrestrial CDOM in the Singapore Strait may again be subject to higher rates of photooxidation during the drier intermonsoon season. However, the seasonal patterns discerned in our space-borne images reinforce the year-round accumulation of organic matter from peat-draining rivers in Sumatran coastal waters.

Sediment composition of Singapore Strait waters

High concentrations of suspended sediments are typical in Sumatran coastal waters (Figures 4–6, Supplementary Figure S2), where particles may consist of either: (1) discharged from Sumatran rivers in copious amounts (2) resuspended bottom sediments, or (3) shore-eroded particles. Sediment concentrations along the Sumatran coastal belt typically decrease offshore (Figures 4–6, Supplementary Figure S2) as the buoyancy settles the mineral-rich particles to the seafloor beyond river plumes within a short distance of the estuaries. Sediments scatter light efficiently owing to their high refractive index compared to other particulates, and their absorption of light is also quite significant (Babin and Stramski, 2004; Stramski et al., 2004). Consequently, particulate backscattering, b_{bp} (400nm)>1m^{-1} and spectral slope of particulate backscattering, η(779-865nm)>1nm^{-1} were observed in coastal waters (Figures 4–6 and Supplementary Figure S2), and especially nearby river mouths in response to changing particulate (both sediment and phytoplankton) concentrations. However, other characteristics such as particle chemical composition, shape and size, and porosity are also responsible for determining selective absorption and scattering (backscattering efficiency) of light. Higher values of the spectral slope of particulate backscattering η(779-865nm) usually indicative of the finer-sized particles (Slade and Boss, 2015). Size analysis of the settled particles collected from the sediment traps in Singapore Strait indicates that sediments exhibited a typically bimodal distribution with a lower peak at 7 µm (fine silt) and a secondary peak at 250 µm (fine sand) (Morgan et al., 2020). Only trace amounts of silt particles (1-7% of total sediment) were quantified with a mean particle size of 9.51-15.5 µm (average: 13.2 ± 2.5 µm) (Morgan et al., 2020). Finer particles offer a large surface area for photon interaction, significantly increasing light scattering (Kirk, 1985), (Kirk, 2010), which explains the observed values of b_{bp}(400nm) >1 m^{-1} in conjunction with η(779-865nm)>1 nm^{-1} (Figures 4, 5 and Supplementary Figure S2). XRD analysis of these sediments demonstrates that particles were primarily siliciclastic and comprised predominately of quartz (SiO_2) with lower amounts of calcium sulfide and a minor fraction of kaolinite and calcium carbonate (Morgan et al., 2020). These terrestrially-derived mineral particles can dominate the optical and attenuation properties of the marine waters by scattering the photosynthetically important blue-green wavelengths, except for iron-rich minerals that absorb rather than scatter the shorter wavelengths (Babin and Stramski, 2004). The suspended particle pool in the Singapore Strait appears to be dominated by inorganic suspended matter (Tanzil et al., 2019) and the suspended organic pool likely contains a significant contribution from organic particles (Morgan et al., 2020; Martin et al., 2022). Non-algal mineral sediments and organic detritus absorb the shorter UV+blue wavelengths, exponentially decreasing towards the longer red wavelengths (Kirk, 1985), (Kirk, 2010). The contribution of suspended sediment concentrations from the local river discharge in the Singapore Strait during the northeast monsoon is negligible due to the dilution by the strong monsoon currents (van Maren et al., 2014). Thus, a relatively minor increase is detected during the northeast monsoon compared to the inter-monsoon periods (Figure 5 and Supplementary Figure S2).

Impact on underwater light penetration

The seasonal variability in the concentrations of -chlorophyll-*a*, suspended sediments, and CDOM, determines the amount and quality of light penetrating through seawater. Our observations from Sunda shelf waters show that the rapid light attenuation by these components vertically compressed the total depth range of light penetration over which photosynthesis can occur. Our data reveals that a 5-10 fold increase in the terrigenous matter is accountable for reducing the Z_d(490) by 9m (45%) for Singapore Strait waters, by 8m (40%) for the Malacca Strait waters, and by 3m (57%) for the Sumatran coastal waters (Figures 4, 5, Supplementary Figure S6) during the southwest monsoon. Previous studies have also reported strong vertical extinction of PAR in the Singapore Strait, consistent with our findings (Dikou and van Woesik, 2006; Chow et al., 2019; Morgan et al., 2020). The relative contributions of the individual components to the light attenuation coefficient K_d (Figure 7) aids in determining the intensity and biogeochemical processes involved in altering the spectral quality of the underwater light field (Lee et al., 2015; Cairo et al., 2016; Gomes et al., 2020). Predominantly, the relative contribution of backscattering from particles to the light attenuation was always higher than that of the CDOM absorption in coastal waters (Figure 7). However, a relatively smaller seasonal variation in particulate backscattering (b_{bp}) in comparison to a_g(400nm) suggests that although sediments contributed significantly to light attenuation, variations in terrigenous CDOM are the main driver for seasonal fluctuations in K_d values (Figure 7). This finding allows us to conclude that the dominant component responsible for the light attenuation is not necessarily also a controlling factor for the seasonal variation of the light attenuation. Although sediment is not the primary driver of light limitation in Sunda shelf waters, their seasonal secondary effects on ecosystem health, for example smothering of benthos, transport of pollutants, physical

abrasion, disease vectors (Morgan et al., 2020) cannot be neglected.

The accumulation of the optically active constituents can cause the euphotic zone to shoal (Aksnes et al., 2009), restricting the abundance and distribution of photosynthetic organisms and their contribution to oceanic and benthic primary production (Gattuso et al., 2006). Correspondingly, absorption by the phytoplankton for our region was consistently lower (<20%) and tended to decrease during periods of higher K_d values. The reduced light availability induced by terrestrial CDOM, also known as "browning" in freshwater systems and "coastal darkening" in marine environments such as North Sea (Granéli, 2012; Dupont and Aksnes, 2013; Capuzzo et al., 2015) has been reported to promote adverse shifts in phytoplankton species composition with the consequences propagating to the zooplankton level and impacting the wider food web such as in the North Sea and in northern Pennsylvania lakes (Mustaffa et al., 2020; Williamson et al., 2020). Coastal darkening caused by increased terrestrial CDOM in Norwegian fjords possibly resulted in mesopelagic shifts from fish to jellyfish (Aksnes et al., 2009). Similarly, an increase in terrigenous organic matter in Southern Norway was found to be a contributing factor to collapsing of kelp forests (Frigstad et al., 2013). The coastal browning has caused a shift in the timing of the spring phytoplankton bloom by up to three weeks in the North Sea (Opdal et al., 2019). Light reduction due to sediment resuspension events are a frequent phenomenon in the coral reef zone of the inner Great Barrier reef (Bessell-Browne et al., 2017; Jones et al., 2021). Sensitive organisms such as corals and crustose coralline algae in the inner Great Barrier reef have been reported to suffer tissue discoloration (bleaching) and partial mortality in just 3–5 days in response to darkness (Yonge and Nicholls, 1931; Titlyanov et al., 2001; Bessell-Browne et al., 2017). Hence, the accumulation of terrestrially-derived CDOM, DOC, and sediments effectively constrain the light budget and hamper productivity in Sunda shelf waters.

Moreover, the seasonal heterogeneity of these optically active water constituents alters the spectral quality of the underwater light (Figure 8), exhibiting a seasonal decline in the availability of blue light relative to longer wavelengths. The most likely biological consequences of poor spectral quality of light in an aquatic system restrict the sustenance of the phytoplankton communities at various depths. These photosynthetic organisms have a narrow range of blue and blue-green wavelengths to absorb effectively (Prieur and Sathyendranath, 1981). The implications of light scarcity may propagate to higher trophic levels and impact the ecosystem function (Brandao et al., 2017). Policymakers require two kinds of information for coastal and offshore planning. Firstly, they need information on the spatial extent of marine resources at risk due to the photic zone compression for a vulnerable aquatic body. Secondly, they need information on exposure timings during which an aquatic body is susceptible to light limitation. A vulnerability assessment performed here helped us identify significant issues associated with the negative consequences of compression in the photic zone (Figure 10). Rapid loss of red and longer wavelengths of PAR in clear marine waters (Kirk, 2010) promoted the propagation of higher-energy blue light in the South China Sea (Figure 8) for $Z_d(490)$ >20m in all the seasons (Figure 4, Supplementary Figure S6), which is beneficial for the well-being of the composition and health of the phytoplankton community (Figure 10A). An adequate amount of light available for planktonic and benthic communities implies that the clear marine waters are not vulnerable to light as a liming factor (VI<0.2, Figure 9) in any season. Preferential loss of red light is accompanied by the intense attenuation of photosynthetically beneficial blue light by CDOM (Fichot and Benner, 2012) and inorganic sediments (Kirk, 2010) influenced waters. The net effect of the attenuation at both ends of the PAR spectrum resulted in shifting the underwater light spectrum towards less suitable green-yellow wavelengths >560nm in most parts of the Malacca Strait and Singapore Strait waters (Figure 8). Hence, the presence of the optically active constituents in these waters shifts the wavelength of maximum light penetration to ~560nm, which is only sufficient to sustain photosynthesis within the photic zone ≤15m (Figures 9, 10B). Subsequently, the medium vulnerability (VI=0.4-0.6, Figure 9) prevails in most parts of Malacca coastal waters and eastern Singapore Strait during the inter-monsoon and northeast Monsoon seasons (Supplementary Figure S7). Phytoplankton in Singapore Strait appear to adjust their pigment composition in response to the changing light environment during the southwest monsoon (Martin et al., 2021). However, the effective penetration of blue-green light conducive to photosynthesis is restricted to ≤10m (Supplementary Figure S6) in the coastal waters and southern part of Malacca Strait and are hence identified as having high range of vulnerability (VI=0.6-0.8, Figure 9).

The Sumatran peat-influenced terrestrial inputs resulted in shifting the underwater light spectrum of coastal waters from photosynthetically valuable to less suitable wavelengths ≥650nm (Figure 8). Elevated scattering by mineral-rich terrigenous sediments, besides increasing the blue-green absorption (Babin and Stramski, 2004), also amplifies the pathlength of light underwater, thereby significantly increasing the probability of UV-blue light absorption by CDOM (Kirk, 1985). Consequently, 95% of light is attenuated within the top few meters (≤5m, Figure 4, Supplementary Figure S6) by the extensive influence of riverine discharges in the Sumatran estuarine and coastal environments. In addition, the Sumatran coastal water belt (Figure 1) and extending offshore waters are year-round (in all the seasons) in a state of high attenuation $K_d(490nm)$>1.5 (Supplementary Figure S5) and year-round, the photic zone, Z_d (490), is limited to ≤5m (Supplementary Figure S6). Consequently, these peat-influenced coastal waters and the

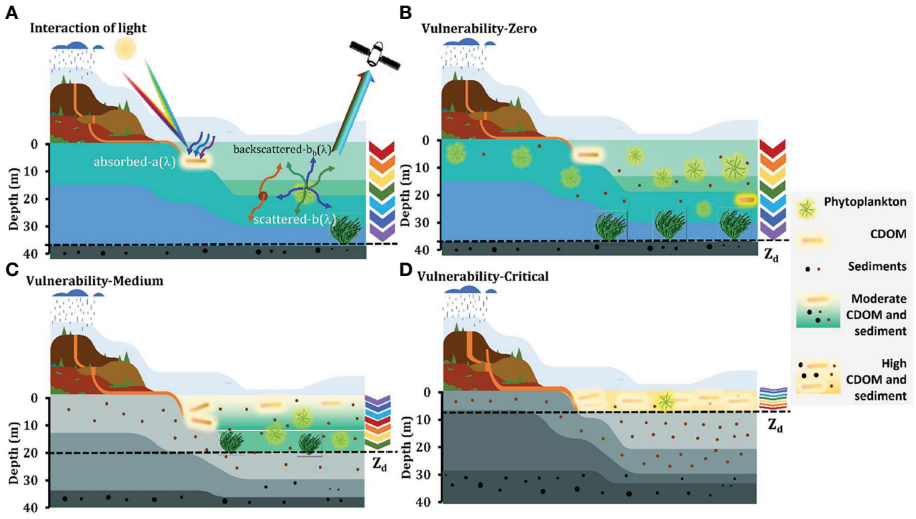

FIGURE 10
Schematic diagram of vulnerability conditions demonstrating photic zone compression and the response of photosynthetic communities to the enrichment of CDOM and sediments in the coastal water column. Panels show **(A)** Interaction of light in a water column, **(B)** low vulnerability state in naturally turbid waters, **(C)** medium vulnerability state in moderately high CDOM and sediment waters, and **(D)** critically high vulnerability state in heavily CDOM-rich and sediment-laden waters.

southern Malacca Strait are critically vulnerable (VI>0.8, Figure 9) to compression of the photic zone and are less conducive for photosynthetic organisms and sustaining primary production (Figure 10D). The persistent light limitation has been observed to lower the seagrass productivity and has accelerated substantial loss of its habitats (Orth et al., 2006; Ralph et al., 2007; Waycott et al., 2009). Areas near the river mouths identified with VI>0.8 and $Z_d(490)$ limited to ≤2km will not likely be colonized by photosynthetic benthic habitats and hence are less cause of concern than the areas >2 km away from the coastline. Photic zone, $Z_d(490)$ for Sumatran coastal water column (2 km away from coastline) is further reduced to ≤3m during the southwest monsoon (Supplementary Figure S6), influencing the Malacca and Singapore Strait (Supplementary Figure S6). The underwater light spectrum in the southern Malacca Strait and eastern Singapore strait waters is shifted to longer wavelengths ≥620nm (Figure 8) during the southwest monsoon due to the enrichment of organic matter and sediments. Consequently, a critically high vulnerable state (VI>0.8, Supplementary Figure S7) is realized in southern Malacca Strait, thereby constraining the photosynthesis to shallower depths ≤5m (Supplementary Figure S6, 10D). And the photic zone is compressed to ≤10m in the eastern Singapore Strait, acquiring a high vulnerability status (VI=0.6-0.8, Figure 9) during the season. Nearly 60% of seagrass beds in Southeast Asia are reported to be already declining at an average rate of 10.9% $year^{-1,}$ which includes Sunda shelf seagrass beds located around Singapore and Malaysia (Sudo et al., 2021). Almost 95% of coral reefs in Southeast Asia are threatened, and the Singapore reefs are categorized under high threat levels (Burke et al., 2011). Additionally, contraction in the photic zone from the bottom of the Singapore Strait has been observed, reducing coral habitat availability and possibly driving the coral-species community (Morgan et al., 2020). Further intensification of CDOM, DOC, and sediment inputs in these waters will increase the risk of light reduction that can threaten marine habitat-forming species. A transformation in the vulnerability status of central Malacca Strait from not vulnerable (VI<0.2) to highly vulnerable (VI=0.6-0.8, Supplementary Figure S7) indicates poor underwater light conditions. Monitoring the vulnerability of fragile aquatic systems is critical for understanding the response of biological communities to current and future changes in the underwater light environment.

Conclusions

When coastal water quality declines due to elevated phytoplankton, CDOM, or sediment concentrations, then underwater light availability is significantly reduced. And our knowledge of photic zone compression influencing the marine habitats in tropical shelf seas is still limited. Here, we performed a vulnerability assessment of light extinction for Sunda shelf seawaters of Southeast Asia. We find that the critically vulnerable (VI>0.8) coastal waters (2 km away from coastline),

including Sumatran coastal waters and the sector of southern Malacca Strait waters during the southwest monsoon, are the areas of major concern. Given the proximity of the Singapore Strait to peatlands on Sumatra, the area is deemed at a mid-level of vulnerability but shifts to high vulnerability during the southwest monsoon, when it receives Sumatran peatland-influenced waters. The seasonal change in light availability caused by these terrestrial inputs in the Sunda shelf is sufficiently substantial to promote changes in photo-acclimation by the phytoplankton community (Martin et al., 2021) and the vertical reef compression (Morgan et al., 2020). However, it remains unclear to what extent of 'light limitation' owing to terrigenous CDOM, DOC, and sediments has impacted the primary production and shelf sea ecosystems.

The areas harboring marine ecosystems (e.g., coral reefs and seagrass beds) in the Sunda shelf sea that are sensitive to environmental change are already at the border of the high vulnerability threshold VI=0.6-0.8. Further intensification of CDOM, DOC, and sediments in already high (VI=0.6-0.8) to critically high light vulnerable (VI>0.8) water columns harboring marine ecosystems may drive detrimental impacts on habitat function and lead to ecological redundancy due to an increasing lack of light. Reduction in the underwater light availability, therefore, constitutes a clear risk, and the vulnerable locations where light is extinct within the top few meters require our special attention. Monitoring the quality of light in coastal waters is highly desired for the fate of survival of the underwater ecosystem. This also underscores the need for a complete ecological risk assessment for Southeast Asia in synergy with physical parameters and biodiversity information which would aid in effective marine ecosystem management.

Data availability statement

The original contributions presented in the study are included in the article/Supplementary Material. Further inquiries can be directed to the corresponding author.

Author contributions

Conceptualization: NS and PM; Investigation and Formal remote sensing analysis: NS and EW; Writing – Original draft: NS; Writing – Review and editing: all authors; Funding acquisition and Project administration: PM. All authors contributed to the article and approved the submitted version.

Funding

Fieldwork was carried out under permit NP/RP17-044-2 from the Singapore National Parks Board. This research was supported by the National Research Foundation Singapore, Prime Minister's Office, under the Marine Science Research and Development Program through grant MSRDP-P32 and MSRDP-P11 to PM.

Acknowledgments

Location of Sumatran Peatland has been adopted from (Wahyunto and Subagjo, 2003) and the Malaysian peatlands are from Global Forest Watch under http://data.globalforestwatch.org/datasets/8d8462fca7b74b298598490b85d3bd44_9/data?geometry=96.470%2C0.845%2C118.607%2C4.685.

Conflict of interest

The authors declare that the research was conducted in the absence of any commercial or financial relationships that could be construed as a potential conflict of interest.

Publisher's note

Supplementary material

The Supplementary Material for this article can be found online at: https://www.frontiersin.org/articles/10.3389/fmars.2022.967627/full#supplementary-material

References

Aksnes, D. L., Dupont, N., Staby, A., Fiksen, Ø., Kaartvedt, S., and Aure, J. (2009). Coastal water darkening and implications for mesopelagic regime shifts in Norwegian fjords. *Mar. Ecol. Prog. Ser.* 387, 39–49. doi: 10.3354/meps08120

Alkhatib, M., Jennerjahn, T. C., and Samiaji, J. (2007). Biogeochemistry of the dumai river estuary, Sumatra, Indonesia, a tropical black-water river. *Limnology Oceanography* 52, 2410–2417. doi: 10.4319/lo.2007.52.6.2410

Ambarwulan, W., Salama, M. S., Mannaerts, C. M., and Verhoef, W. (2010). Estimating specific inherent optical properties of tropical coastal waters using bio-optical model inversion and *in situ* measurements: case of the berau estuary, East kalimantan, Indonesia. *Hydrobiologia* 658, 197–211. doi: 10.1007/s10750-010-0473-7

Aurin, D. A., Dierssen, H. M., Twardowski, M. S., and Roesler, C. S. (2010). Optical complexity in long island sound and implications for coastal ocean color remote sensing. *J. Geophysical Res.* 115, C07011. doi: 10.1029/2009JC005837

Aurin, D., Mannino, A., and Lary, D. J. (2018). Remote sensing of CDOM, CDOM spectral slope, and dissolved organic carbon in the global ocean. *Appl. Sci. (Basel)* 8, 2687. doi: 10.3390/app8122687

Babin, M. (2003). Variations in the light absorption coefficients of phytoplankton, nonalgal particles, and dissolved organic matter in coastal waters around Europe. *J. Geophysical Res.* 108, C7. doi: 10.1029/2001JC000882

Babin, M., and Stramski, D. (2004). Variations in the mass-specific absorption coefficient of mineral particles suspended in water. *Limnology Oceanography* 49, 756–767. doi: 10.4319/lo.2004.49.3.0756

Baum, A., Rixen, T., and Samiaji, J. (2007). Relevance of peat draining rivers in central Sumatra for the riverine input of dissolved organic carbon into the ocean. *Estuarine Coast. Shelf Sci.* 73, 563–570. doi: 10.1016/j.ecss.2007.02.012

Bessell-Browne, P., Negri, A. P., Fisher, R., Clode, P. L., and Jones, R. (2017). Impacts of light limitation on corals and crustose coralline algae. *Sci. Rep.* 7, 11553. doi: 10.1038/s41598-017-11783-z

Boss, E., and Behrenfeld, M. (2010). *In situ* evaluation of the initiation of the north Atlantic phytoplankton bloom. *Geophysical Res. Lett.* 37, n/a–n/a. doi: 10.1029/2010GL044174

Bowers, D. G., Md-Suffian, I., and Mitchelson-Jacob, E. G. (2011). Bio-optical properties of east coast Malaysia waters in relation to remote sensing of chlorophyll. *Int. J. Remote Sens.* 33, 150–169. doi: 10.1080/01431161.2011.584917

Brandao, L. P. M., Brighenti, L. S., Staehr, P. A., Barbosa, F. A. R., and Bezerra-Neto, J. F. (2017). Partitioning of the diffuse attenuation coefficient for photosynthetically available irradiance in a deep dendritic tropical lake. *Acad. Bras. Cienc* 89, 469–489. doi: 10.1590/0001-3765201720160016

Burke, L., Reytar, K., Spalding, M., and Perry, A. (2011). *Reefs at risk revisited* (Washington, DC: World Resources Institute).

Cairo, C. T., Barbosa, C. C. F., de Moraes Novo, E. M. L., and do Carmo Calijuri, M. (2016). Spatial and seasonal variation in diffuse attenuation coefficients of downward irradiance at ibitinga reservoir, são paulo, Brazil. *Hydrobiologia* 784, 265–282. doi: 10.1007/s10750-016-2883-7

Cao, F., Tzortziou, M., Hu, C., Mannino, A., Fichot, C. G., Del Vecchio, R., et al. (2018). Remote sensing retrievals of colored dissolved organic matter and dissolved organic carbon dynamics in north American estuaries and their margins. *Remote Sens. Environ.* 205, 151–165. doi: 10.1016/j.rse.2017.11.014

Capuzzo, E., Stephens, D., Silva, T., Barry, J., and Forster, R. M. (2015). Decrease in water clarity of the southern and central north Sea during the 20th century. *Glob Chang Biol.* 21, 2206–2214. doi: 10.1111/gcb.12854

Carmona, F., Rivas, R., and Fonnegra, D. C. (2017). Vegetation index to estimate chlorophyll content from multispectral remote sensing data. *Eur. J. Remote Sens.* 48, 319–326. doi: 10.5721/EuJRS20154818

Chen, J., He, X., Zhou, B., and Pan, D. (2017). Deriving colored dissolved organic matter absorption coefficient from ocean color with a neural quasi-analytical algorithm. *J. Geophysical Research: Oceans* 122, 8543–8556. doi: 10.1002/2017JC013115

Chen, J., Wen, Z., and Xiao, Z. (2011). Spectral geometric triangle properties of chlorophyll-a inversion in taihu lake based on TM data. *J. Water Resource Prot.* 03, 67–75. doi: 10.4236/jwarp.2011.31008

Cherukuru, N., Martin, P., Sanwlani, N., Mujahid, A., and Müller, M. (2020). A semi-analytical optical remote sensing model to estimate suspended sediment and dissolved organic carbon in tropical coastal waters influenced by peatland-draining river discharges off Sarawak, Borneo. *Remote Sens.* 13, 99. doi: 10.3390/rs13010099

Chow, G. S. E., Chan, Y. K. S., Jain, S. S., and Huang, D. (2019). Light limitation selects for depth generalists in urbanised reef coral communities. *Mar. Environ. Res.* 147, 101–112. doi: 10.1016/j.marenvres.2019.04.010

Coble, P. G. (2007). Marine optical biogeochemistry: the chemistry of ocean color. *Chem. Rev.* 107, 402–418. doi: 10.1021/cr050350+

Delegido, J., Alonso, L., González, G., and Moreno, J. (2010). Estimating chlorophyll content of crops from hyperspectral data using a normalized area over reflectance curve (NAOC). *Int. J. Appl. Earth Observation Geoinformation* 12, 165–174. doi: 10.1016/j.jag.2010.02.003

Delegido, J., Vergara, C., Verrelst, J., Gandia, S., and Moreno, J. (2011). Remote estimation of crop chlorophyll content by means of high-Spectral-Resolution reflectance techniques. *Agron. J.* 103, 1834–1842. doi: 10.2134/agronj2011.0101

Dikou, A., and van Woesik, R. (2006). Survival under chronic stress from sediment load: Spatial patterns of hard coral communities in the southern islands of Singapore. *Mar. pollut. Bull.* 52, 7–21. doi: 10.1016/j.marpolbul.2005.07.021

Dommain, R., Couwenberg, J., Glaser, P. H., Joosten, H., and Suryadiputra, I. N. N. (2014). Carbon storage and release in Indonesian peatlands since the last deglaciation. *Quaternary Sci. Rev.* 97, 1–32. doi: 10.1016/j.quascirev.2014.05.002

Doxaran, D., Cherukuru, N., and Lavender, S. J. (2006). Apparent and inherent optical properties of turbid estuarine waters: measurements, empirical quantification relationships, and modeling. *Appl. Optics* 45, 2310–2324. doi: 10.1364/AO.45.002310

Dupont, N., and Aksnes, D. L. (2013). Centennial changes in water clarity of the Baltic Sea and the north Sea. *Estuarine Coast. Shelf Sci.* 131, 282–289. doi: 10.1016/j.ecss.2013.08.010

Fargion, G. S., and Mueller, J. L. (2000). *Ocean optics protocols for satellite ocean color sensor validation* (Greenbelt, Maryland: National Aeronautical and Space Administration, Goddard Space Flight Center).

Ferrari, G. M., and Tassan, S. (1999). A method using chemical oxidation to remove light absorption by phytoplankton pigments. *J. Phycology* 35, 1090–1098. doi: 10.1046/j.1529-8817.1999.3551090.x

Fichot, C. G., and Benner, R. (2012). The spectral slope coefficient of chromophoric dissolved organic matter (S275-295) as a tracer of terrigenous dissolved organic carbon in river-influenced ocean margins. *Limnology Oceanography* 57, 1453–1466. doi: 10.4319/lo.2012.57.5.1453

Fichot, C. G., and Benner, R. (2014). The fate of terrigenous dissolved organic carbon in a river-influenced ocean margin. *Global Biogeochem Cycles* 28, 300–318. doi: 10.1002/2013GB004670

Fichot, C. G., Kaiser, K., Hooker, S. B., Amon, R. M., Babin, M., Belanger, S., et al. (2013). Pan-Arctic distributions of continental runoff in the Arctic ocean. *Sci. Rep.* 3, 1053. doi: 10.1038/srep01053

Fredston-Hermann, A., Brown, C. J., Albert, S., Klein, C. J., Mangubhai, S., Nelson, J. L., et al. (2016). Where does river runoff matter for coastal marine conservation? *Front. Mar. Sci.* 3. doi: 10.3389/fmars.2016.00273

Frigstad, H., Andersen, T., Hessen, D. O., Jeansson, E., Skogen, M., Naustvoll, L.-J., et al. (2013). Long-term trends in carbon, nutrients and stoichiometry in Norwegian coastal waters: Evidence of a regime shift. *Prog. Oceanography* 111, 113–124. doi: 10.1016/j.pocean.2013.01.006

Gattuso, J. P., Gentili, B., Duarte, C. M., Kleypas, J. A., Middelburg, J. J., and Antoine, D. (2006). Light availability in the coastal ocean: impact on the distribution of benthic photosynthetic organisms and their contribution to primary production. *Biogeosciences* 3, 489–513. doi: 10.5194/bg-3-489-2006

Gitelson, A. A. (2005). Remote estimation of canopy chlorophyll content in crops. *Geophysical Res. Lett.* 32, L08403. doi: 10.1029/2005GL022688

Gomes, A. C., Alcântara, E., Rodrigues, T., and Bernardo, N. (2020). Satellite estimates of euphotic zone and secchi disk depths in a colored dissolved organic matter-dominated inland water. *Ecol. Indic.* 110, 105848. doi: 10.1016/j.ecolind.2019.105848

Gordon, A. (2005). Oceanography of the Indonesian seas and their throughflow. *Oceanography* 18, 14–27. doi: 10.5670/oceanog.2005.01

Gordon, H. R., Brown, O. B., and Jacobs, M. M. (1975). Computed relationships between the inherent and apparent optical properties of a flat homogeneous ocean. *Appl. Opt* 14, 417–427. doi: 10.1364/AO.14.000417

Gordon, A. L., Huber, B. A., Metzger, E. J., Susanto, R. D., Hurlburt, H. E., and Adi, T. R. (2012). South China Sea throughflow impact on the Indonesian throughflow. *Geophysical Res. Lett.* 39, n/a–n/a. doi: 10.1029/2012GL052021

Granéli, W. (2012). *Encyclopedia of lakes and reservoirs* (Dordrecht, Heidelberg, New York, London: Springer).

Harvey, G. R., Boran, D. A., Chesal, L. A., and Tokar, J. M. (1983). The structure of marine fulvic and humic acids. *Mar. Chem.* 12, 119–132. doi: 10.1016/0304-4203(83)90075-0

Helms, J. R., Stubbins, A., Ritchie, J. D., Minor, E. C., Kieber, D. J., and Mopper, K. (2008). Absorption spectral slopes and slope ratios as indicators of molecular weight, source, and photobleaching of chromophoric dissolved organic matter. *Limnology Oceanography* 53, 955–969. doi: 10.4319/lo.2008.53.3.0955

Heiri, O., Lotter, A. F., and Lemcke, G. (2001). Loss on ignition as a method for estimating organic and carbonate content in sediments: reproducibility and comparability of results. *J. Paleolimnol.* 25, 101–110. doi: 10.1023/A:1008119611481

Hu, C., Lee, Z., and Franz, B. (2012). Chlorophyll a algorithms for oligotrophic oceans: A novel approach based on three-band reflectance difference. *J. Geophysical Research: Oceans* 117 (C1), C01011. doi: 10.1029/2011JC007395

IOCCG (2006). *Remote sensing of inherent optical properties: Fundamentals, tests of algorithms, and applications* (Dartmouth, Canada: Reports of the International Ocean-Colour Coordinating Group (IOCCG).

Jones, R., Pineda, M.-C., Luter, H. M., Fisher, R., Francis, D., Klonowski, W., et al. (2021). Underwater light characteristics of turbid coral reefs of the inner central great barrier reef. *Front. Mar. Sci.* 8. doi: 10.3389/fmars.2021.727206

Joshi, I. D., D'Sa, E. J., Osburn, C. L., Bianchi, T. S., Ko, D. S., Oviedo-Vargas, D., et al. (2017). Assessing chromophoric dissolved organic matter (CDOM) distribution, stocks, and fluxes in Apalachicola bay using combined field, VIIRS ocean color, and model observations. *Remote Sens. Environ.* 191, 359–372. doi: 10.1016/j.rse.2017.01.039

Kirk, J. T. O. (1984). Dependence of relationship between inherent and apparent optical properties of water on solar altitude. *Limnology Oceanography* (Cambridge: Cambridge University Press) 29, 350–356. doi: 10.4319/lo.1984.29.2.0350

Kirk, J. T. O. (1985). Effects of suspensoids (turbidity) on penetration of solar radiation in aquatic ecosystems. *Hydrobiologia* 125, 195–208. doi: 10.1007/BF00045935

Kirk, J. T. O. (1994). *Light and photosynthesis in aquatic ecosystems* (Cambridge: Cambridge University Press).

Kirk, J. T. O. (2010). *Light and photosynthesis in aquatic ecosystems* (Cambridge: Cambridge University Press).

Kramer, N., Tamir, R., Eyal, G., and Loya, Y. (2020). Coral morphology portrays the spatial distribution and population size-structure along a 5–100 m depth gradient. *Front. Mar. Sci.* 7. doi: 10.3389/fmars.2020.00615

Lee, Z., Carder, K. L., and Arnone, R. A. (2002). Deriving inherent optical properties from water color: a multiband quasi-analytical algorithm for optically deep waters. *Appl. Opt* 41, 5755–5772. doi: 10.1364/AO.41.005755

Lee, Z.-P., Du, K.-P., and Arnone, R. (2005). A model for the diffuse attenuation coefficient of downwelling irradiance. *J. Geophysical Res.* 110. doi: 10.1029/2004JC002275

Lee, Z., Shang, S., Du, K., Wei, J., and Arnone, R. (2014). Usable solar radiation and its attenuation in the upper water column. *J. Geophysical Research: Oceans* 119, 1488–1497. doi: 10.1002/2013JC009507

Lee, Z., Shang, S., Hu, C., Du, K., Weidemann, A., Hou, W., et al. (2015). Secchi disk depth: A new theory and mechanistic model for underwater visibility. *Remote Sens. Environ.* 169, 139–149. doi: 10.1016/j.rse.2015.08.002

Liu, B., D'Sa, E. J., and Joshi, I. (2019). Multi-decadal trends and influences on dissolved organic carbon distribution in the barataria basin, Louisiana from *in-situ* and Landsat/MODIS observations. *Remote Sens. Environ.* 228, 183–202. doi: 10.1016/j.rse.2019.04.023

Mannino, A., Novak, M. G., Hooker, S. B., Hyde, K., and Aurin, D. (2014). Algorithm development and validation of CDOM properties for estuarine and continental shelf waters along the northeastern U.S. coast. *Remote Sens. Environ.* 152, 576–602. doi: 10.1016/j.rse.2014.06.027

Martin, P., Cherukuru, N., Tan, A. S. Y., Sanwlani, N., Mujahid, A., and Müller, M. (2018). Distribution and cycling of terrigenous dissolved organic carbon in peatland-draining rivers and coastal waters of Sarawak, Borneo. *Biogeosciences* 15, 6847–6865. doi: 10.5194/bg-15-6847-2018

Martin, P., Moynihan, M. A., Chen, S., Woo, O. Y., Zhou, Y., Nichols, R. S., et al. (2022). Monsoon-driven biogeochemical dynamics in an equatorial shelf sea: Time-series observations in the Singapore strait. *Estuarine Coast. Shelf Sci.* 270, 107855. doi: 10.1016/j.ecss.2022.107855

Martin, P., Sanwlani, N., Lee, T. W. Q., Wong, J. M. C., Chang, K. Y. W., Wong, E. W. S., et al. (2021). Dissolved organic matter from tropical peatlands reduces shelf sea light availability in the Singapore strait, southeast Asia. *Mar. Ecol. Prog. Ser.* 672, 89–109. doi: 10.3354/meps13776

Massicotte, P., and Frenette, J. J. (2011). Spatial connectivity in a large river system: resolving the sources and fate of dissolved organic matter. *Ecol. Appl.* 21, 2600–2617. doi: 10.1890/10-1475.1

Miettinen, J., Shi, C., and Liew, S. C. (2016). Land cover distribution in the peatlands of peninsular Malaysia, Sumatra and Borneo in 2015 with changes since 1990. *Global Ecol. Conserv.* 6, 67–78. doi: 10.1016/j.gecco.2016.02.004

Moore, S., Evans, C. D., Page, S. E., Garnett, M. H., Jones, T. G., Freeman, C., et al. (2013). Deep instability of deforested tropical peatlands revealed by fluvial organic carbon fluxes. *Nature* 493, 660–663. doi: 10.1038/nature11818

Moore, S., Gauci, V., Evans, C. D., and Page, S. E. (2011). Fluvial organic carbon losses from a bornean blackwater river. *Biogeosciences* 8, 901–909. doi: 10.5194/bg-8-901-2011

Morgan, K. M., Moynihan, M. A., Sanwlani, N., and Switzer, A. D. (2020). Light limitation and depth-variable sedimentation drives vertical reef compression on turbid coral reefs. *Front. Mar. Sci.* 7. doi: 10.3389/fmars.2020.571256

Müller-Dum, D., Warneke, T., Rixen, T., Müller, M., Baum, A., Christodoulou, A., et al. (2019). Impact of peatlands on carbon dioxide (CO<sub<2</sub<) emissions from the rajang river and estuary, Malaysia. *Biogeosciences* 16, 17–32. doi: 10.5194/bg-16-17-2019

Mustaffa, N. I. H., Kallajoki, L., Biederbick, J., Binder, F. I., Schlenker, A., and Striebel, M. (2020). Coastal ocean darkening effects *via* terrigenous DOM addition on plankton: An indoor mesocosm experiment. *Front. Mar. Sci.* 7. doi: 10.3389/fmars.2020.547829

Nelson, N. B., and Siegel, D. A. (2013). The global distribution and dynamics of chromophoric dissolved organic matter. *Ann. Rev. Mar. Sci.* 5, 447–476. doi: 10.1146/annurev-marine-120710-100751

Nichols, R. S., and Martin, P. (2021). Low biodegradability of dissolved organic matter from southeast Asian peat-draining rivers. *J. Geophysical Research: Biogeosciences* 126, e06182. doi: 10.1029/2020JG006182

Oestreich, W. K., Ganju, N. K., Pohlman, J. W., and Suttles, S. E. (2016). Colored dissolved organic matter in shallow estuaries: relationships between carbon sources and light attenuation. *Biogeosciences* 13, 583–595. doi: 10.5194/bg-13-583-2016

Opdal, A. F., Lindemann, C., and Aksnes, D. L. (2019). Centennial decline in north Sea water clarity causes strong delay in phytoplankton bloom timing. *Global Change Biol.* 25, 3946–3953. doi: 10.1111/gcb.14810

Orth, R. J., Carruthers, T. J. B., Dennison, W. C., Duarte, C. M., Fourqurean, J. W., Heck, K. L., et al. (2006). A global crisis for seagrass ecosystems. *BioScience* 56, 987–996. doi: 10.1641/0006-3568(2006)56[987:AGCFSE]2.0.CO;2

Oubelkheir, K., Clementson, L. A., Webster, I. T., Ford, P. W., Dekker, A. G., Radke, L. C., et al. (2006). Using inherent optical properties to investigate biogeochemical dynamics in a tropical macrotidal coastal system. *J. Geophysical Res.* 111, C7. doi: 10.1029/2005JC003113

Page, S. E., Rieley, J. O., and Banks, C. J. (2011). Global and regional importance of the tropical peatland carbon pool. *Global Change Biol.* 17, 798–818. doi: 10.1111/j.1365-2486.2010.02279.x

Pienitz, R., and Vincent, W. F. (2000). Effect of climate change relative to ozone depletion on UV exposure in subarctic lakes. *Nature* 404, 484–487. doi: 10.1038/35006616

Prieur, L., and Sathyendranath, S. (1981). An optical classification of coastal and oceanic waters based on the specific spectral absorption curves of phytoplankton pigments, dissolved organic matter, and other particulate materials1. *Limnology Oceanography* 26, 671–689. doi: 10.4319/lo.1981.26.4.0671

Ralph, P. J., Durako, M. J., Enríquez, S., Collier, C. J., and Doblin, M. A. (2007). Impact of light limitation on seagrasses. *J. Exp. Mar. Biol. Ecol.* 350, 176–193. doi: 10.1016/j.jembe.2007.06.017

Rixen, T., Baum, A., Pohlmann, T., Balzer, W., Samiaji, J., and Jose, C. (2008). The siak, a tropical black water river in central Sumatra on the verge of anoxia. *Biogeochemistry* 90, 129–140. doi: 10.1007/s10533-008-9239-y

Rixen, T., Baum, A., Wit, F., and Samiaji, J. (2016). Carbon leaching from tropical peat soils and consequences for carbon balances. *Front. Earth Sci.* 4. doi: 10.3389/feart.2016.00074

Sanwlani, N., Evans, C. D., Müller, M., Cherukuru, N. R. C., and Martin, P. (2022). Rising dissolved organic carbon concentrations in southeast Asian coastal waters. *Sci. Adv.* 8(15), eabi5688. doi: 10.1126/sciadv.abi5688

Shanmugam, P. (2011). New models for retrieving and partitioning the colored dissolved organic matter in the global ocean: Implications for remote sensing. *Remote Sens. Environ.* 115, 1501–1521. doi: 10.1016/j.rse.2011.02.009

Shi, W., and Wang, M. (2019). A blended inherent optical property algorithm for global satellite ocean color observations. *Limnology Oceanography: Methods* 17, 377–394. doi: 10.1002/lom3.10320

Siegel, H., Gerth., M., Stottmeister, I., Baum, A., and Samiaji, J. (2019). *Remote sensing of coastal discharge of SE Sumatra (Indonesia)* (Cham: Springer). pp. 359–376.

Signorini, S. R., Mannino, A., Friedrichs, M. A. M., St-Laurent, P., Wilkin, J., Tabatabai, A., et al. (2019). Estuarine dissolved organic carbon flux from space: With application to Chesapeake and Delaware bays. *J. Geophysical Research: Oceans* 124, 3755–3778. doi: 10.1029/2018JC014646

Slade, W. H., and Boss, E. (2015). Spectral attenuation and backscattering as indicators of average particle size. *Appl. Opt* 54, 7264–7277. doi: 10.1364/AO.54.007264

Stramski, D., Reynolds, R. A., Kaczmarek, S., Uitz, J., and Zheng, G. (2015). Correction of pathlength amplification in the filter-pad technique for measurements of particulate absorption coefficient in the visible spectral region. *Appl. Opt* 54, 6763–6782. doi: 10.1364/AO.54.006763

Stramski, D., Woźniak, S. B., and Flatau, P. J. (2004). Optical properties of Asian mineral dust suspended in seawater. *Limnology Oceanography* 49, 749–755. doi: 10.4319/lo.2004.49.3.0749

Sudo, K., Quiros, T. E. A. L., Prathep, A., Luong, C. V., Lin, H.-J., Bujang, J. S., et al. (2021). Distribution, temporal change, and conservation status of tropical seagrass beds in southeast Asia: 2000–2020. *Front. Mar. Sci.* 8. doi: 10.3389/fmars.2021.637722

Tanzil, J. T. I., Goodkin, N. F., Sin, T. M., Chen, M. L., Fabbro, G. N., Boyle, E. A., et al. (2019). Multi-colony coral skeletal Ba/Ca from singapore's turbid urban reefs: Relationship with contemporaneous *in-situ* seawater parameters. *Geochimica Cosmochimica Acta* 250, 191–208. doi: 10.1016/j.gca.2019.01.034

Thushara, V., Vinayachandran, P. N. M., Matthews, A. J., Webber, B. G. M., and Queste, B. Y. (2019). Vertical distribution of chlorophyll in dynamically distinct regions of the southern bay of Bengal. *Biogeosciences* 16, 1447–1468. doi: 10.5194/bg-16-1447-2019

Titlyanov, E. A., Titlyanova, T. V., Yamazato, K., and van Woesik, R. (2001). Photo-acclimation dynamics of the coral stylophora pistillata to low and extremely low light. *J. Exp. Mar. Biol. Ecol.* 263, 211–225. doi: 10.1016/S0022-0981(01)00309-4

Vadrevu, K. P., Lasko, K., Giglio, L., Schroeder, W., Biswas, S., and Justice, C. (2019). Trends in vegetation fires in south and southeast Asian countries. *Sci. Rep.* 9, 7422. doi: 10.1038/s41598-019-43940-x

van Maren, D. S., and Gerritsen, H. (2012). Residual flow and tidal asymmetry in the Singapore strait, with implications for resuspension and residual transport of sediment. *J. Geophysical Research: Oceans* 117, n/a–n/a. doi: 10.1029/2011JC007615

van Maren, D. S., Liew, S. C., and Hasan, G. M. J. (2014). The role of terrestrial sediment on turbidity near singapore's coral reefs. *Continental Shelf Res.* 76, 75–88. doi: 10.1016/j.csr.2013.12.001

Vantrepotte, V., Danhiez, F. P., Loisel, H., Ouillon, S., Meriaux, X., Cauvin, A., et al. (2015). CDOM-DOC relationship in contrasted coastal waters: implication for DOC retrieval from ocean color remote sensing observation. *Opt Express* 23, 33–54. doi: 10.1364/OE.23.000033

Wahyunto, R. S., and Subagjo, H. (2003). "Maps of area of peatland distribution and carbon content in sumatera 1990–2002," in *Wetlands international-Indonesia programme & wildlife habitat Canada (WHC)* (Bogor: Jl. A. Yani No. 53 Bogor 16161 Jawa Barat – INDONESIA).

Waycott, M., Duarte, C. M., Carruthers, T. J., Orth, R. J., Dennison, W. C., Olyarnik, S., et al. (2009). Accelerating loss of seagrasses across the globe threatens coastal ecosystems. *Proc. Natl. Acad. Sci. U. S. A.* 106, 12377–12381. doi: 10.1073/pnas.0905620106

Williamson, C. E., Overholt, E. P., Pilla, R. M., and Wilkins, K. W. (2020). Habitat-mediated responses of zooplankton to decreasing light in two temperate lakes undergoing long-term browning. *Front. Environ. Sci.* 8. doi: 10.3389/fenvs.2020.00073

Wit, F., Muller, D., Baum, A., Warneke, T., Pranowo, W. S., Muller, M., et al. (2015). The impact of disturbed peatlands on river outgassing in southeast Asia. *Nat. Commun.* 6, 10155. doi: 10.1038/ncomms10155

Wit, F., Rixen, T., Baum, A., Pranowo, W. S., and Hutahaean, A. A. (2018). The invisible carbon footprint as a hidden impact of peatland degradation inducing marine carbonate dissolution in Sumatra, Indonesia. *Sci. Rep.* 8, 17403. doi: 10.1038/s41598-018-35769-7

Wyrtki, K. (1961). *Physical oceanography of the southeast Asian waters* (La Jolla, California: The University of California Scripps Institution of Oceanography).

Yonge, C. M., and Nicholls., A. G. (1931). "Studies on the physiology of corals. the effects of starvation in light and in darkness on the relationship between corals and zooxanthellae," in *Great barrier reef expedition 1928-29* (London, BM(NH): British Museum, London (UK) Scientific Reports BritishMuseum (Natural History), 13–57.

Yupi, H. M., Inoue, T., Bathgate, J., and Putra, R. (2016). Concentrations, loads and yields of organic carbon from two tropical peat swamp forest streams in riau province, Sumatra, Indonesia. *Mires Peat* 18, 1–15. doi: 10.19189/MaP.2015.OMB.181

Zhou, Y., Evans, C. D., Chen, Y., Chang, K. Y. W., and Martin, P. (2021). Extensive remineralization of peatland-derived dissolved organic carbon and ocean acidification in the sunda shelf Sea, southeast Asia. *J. Geophysical Research: Oceans* 126, 6. doi.org/10.1029/2021JC017292

Zhou, Y., Martin, P., and Müller, M. (2019). Composition and cycling of dissolved organic matter from tropical peatlands of coastal Sarawak, Borneo, revealed by fluorescence spectroscopy and parallel factor analysis. *Biogeosciences* 16, 2733–2749. doi: 10.5194/bg-16-2733-2019